THESIS

A STUDY ON THE PERMEABILITY AND MECHANICAL CHARACTERISTICS OF CERAMIC SCAFFOLD FOR BONE REGENERATION

Submitted by

Shashank Kanakamedala

Department of Mechanical Engineering

In partial fulfillment of the requirements

For the Degree of Master of Science

Colorado State University

Fort Collins, Colorado

Spring 2026

Master's Committee:
Advisor: David Prawel

Kirk McGilvray
Paul Heyliger

ABSTRACT

A STUDY ON THE PERMEABILITY AND MECHANICAL CHARACTERISTICS OF CERAMIC SCAFFOLD FOR BONE REGENERATION

Large segmental bone defects require scaffolds that provide mechanical stability while enabling bone regeneration. Calcium phosphate ceramics are highly osteoconductive, yet their strength decreases at the high porosities necessary to achieve similar permeability as trabecular bone, since the scaffolds implanted in load bearing defects must simultaneously resist physiological forces and maintain the transport environment required for vascular infiltration and osteogenesis. Triply periodic minimal surface (TPMS) geometries offer advantageous combination of properties: continuous smooth curvature eliminates sharp nodal junction which act as stress concentration in conventional struct-lattice architectures, distributing load more uniformly across scaffold walls and improving specific strength at high porosity while simultaneously fully interconnected porosity preserves the transport environment needed, making them strong candidates for improving this strength and transport trade-off.

To meet the mechanical and biological requirements of load bearing bone defect repair, synthetic scaffolds have been produced from a wide range of materials, including metals like titanium, ceramics such as calcium phosphate based materials, and composites such as bioglass and polymeric blends. Among these calcium phosphate based materials especially hydroxyapatite (HAp) and tricalcium phosphate (TCP) have emerged as preferred choices for bone tissue engineering due to their biocompatibility and high levels of bioactivity including osteoconductivity, osteoinductivity, and osseointegration, compositional similarity to human bone mineral.

While 3D printing of ceramics has shown considerable potential, fabrication and design methodologies remain limited in their ability to produce large-sized scaffolds suitable for load

bearing applications. Hydroxyapatite was therefore selected in the present work as the scaffold material, building directly on prior work in our laboratory that established the compressive mechanical properties of HAp constructs; the present study extends that foundation by incorporating permeability characterization, which had not previously been quantified for these architectures.

The scaffold geometries selected to be studied are Fischer–Koch S (FKS) and Gyroid architectures, which are TPMS structures. Gyroid is the most extensively characterized TPMS topology in the literature and serves as the benchmark geometry against which alternatives are evaluated. The FKS surface, while less studied, presents a distinct channel morphology and pore connectivity pattern that may confer different mechanical and transport behavior at equivalent porosity. Direct experimental comparison between these two topologies under matched fabrication and testing conditions is therefore necessary to determine whether the FKS architecture offers a meaningful advantage.

HAp scaffolds with FKS and Gyroid architectures were fabricated and experimentally characterized for permeability. Permeability was selected as the primary transport metric because it governs interstitial fluid flow, nutrient and oxygen delivery, and the mechanotransductive signals that drive osteogenic differentiation and vascular infiltration; all prerequisites for successful regeneration in a large defect. Both designs exhibited permeabilities on the order of 10^{-9} m^2, consistent with trabecular bone. FKS scaffolds demonstrated significantly greater compressive strength and energy absorption than Gyroid scaffolds despite comparable elastic moduli, indicating that architectural topology influences load redistribution and failure behavior beyond bulk elastic properties alone.

Mechanical performance under clinical fixation was then investigated. Cadaveric studies have shown that fixation hardware transfers substantial load around defect sites, reducing mechanical demand on the scaffold. Quantifying the full multiaxial strain state within a scaffold under clinically representative fixation conditions was therefore necessary to determine whether internal deformations remain within the mechanobiological window compatible with osteogenesis, and to identify whether supplementary mechanical support could reduce the transverse strain components

most likely to drive ceramic failure. To address this, a polycaprolactone (PCL) endoprosthetic sleeve was designed as an external mechanical support strategy. PCL was selected for its biocompatibility, biodegradability, and low temperature processability, which together make it suitable for patient specific fabrication via melt extrusion. Critically, positioning the reinforcing element externally as a sleeve around the scaffold perimeter rather than as an infiltrant within the scaffold matrix was intended to provide mechanical support without occluding the scaffold's pore network or masking its osteoconductive surface, thereby preserving the biological function of the ceramic architecture. Strain distribution was therefore measured in Gyroid scaffold constructs under compressive loading, with and without a PCL endoprosthetic sleeve, using rosette strain gauges in an ovine metatarsal critical defect model. Axial compressive strain remained within the osteogenic range in both conditions. Incorporation of the sleeve significantly reduced transverse strain to approximately 0.3%, representing a reduction of approximately 30% relative to the unsleeved condition, redistributing load around the scaffold perimeter and suppressing localized wall bending without attenuating the axial compressive stimulus. These findings suggest that the external sleeve strategy may decouple structural reinforcement from scaffold bioactivity as our results show that mechanical modulation of the strain environment appears to be achievable independently of scaffold composition, though direct confirmation of preserved bioactivity would require cell based or in vivo validation.

Finite element modeling was implemented to identify and quantify internal stress distributions within the scaffold–bone–sleeve construct that are physically inaccessible to surface mounted strain gauges. Computational analysis confirmed experimental strain trends and established a parametric framework for optimizing sleeve geometry to further influence the distribution of both axial and transverse strain components. This framework provides a basis for optimizing sleeve design to maintain transverse strain below the threshold associated with fibrous tissue formation while preserving axial compressive strain within the range shown to promote and preserve osteogenic axial stimulus.

Collectively, this work demonstrates that TPMS topology governs strength and permeability

balance, that external constraint can strategically modulate the *in vivo* strain environment, and that computational modeling enables rational optimization of coupled mechanical and transport phenomena for safe clinical translation of high porosity ceramic scaffolds in critical defects.

ACKNOWLEDGEMENTS

I would like to express my sincere gratitude to several people without whose contribution and support, the completion of this thesis could not have been possible.

First and foremost, I am profoundly grateful to my advisor, Dr. David Prawel, for his belief in me and for granting me this remarkable opportunity.

I would like to thank my parents Uma and Jitendra Kumar for providing me with all the opportunities that have brought me here and for always supporting my goals. Additionally, thanks to my sister, Shreya as well as my friends for the meaning they give to life.

I would also like to extend my sincerest gratitude to my committee members, Dr. Kirk McGilvray and Dr. Paul Heyliger for their encouragement, support and helpful insights.

I would like to acknowledge my department of Mechanical Engineering for their financial support and assistantship. Special thanks to Amanda, my graduate coordinator, for always standing by my side and for her assistance in resolving issues.

I would also like to thank my lab mates, Oto Durán, Tyler Gerry, Daniel Watling, Vail Baumer, Genesis Marrero, Nelson Isaacson and the whole undergraduate team for all the work they did contributing to this work. It could not have happened without each one of you.I would also like to thank Dr. John Kisiday for donating the Incudyne machine to our lab.

I would also like to thank Dr. V Chandrasekar, Dr. N Saravanakumar, Dr. P. Manoj Kumar for their guidance.

I personally thank Soundarya Sivakumar, Rohan Madhu, Karthick Mohan Kumar, Sudharsan Senthil Kumar, Vishnu Charan Venkatesh, Pradeep Murugan, Akshay Kumar Gunniah, Aishwarya Senthilkumar, Sowmiya Priya Senthilkumar, Pradeep Kumar Loganathan who made me feel at home.

DEDICATION

To my parents, Uma and Jitendra Kumar and to my advisor, Dr. David Prawel for their love, support and sacrifice.

TABLE OF CONTENTS

LIST OF FIGURES

Chapter 1 Introduction

1.1 Clinical Challenge of Load-Bearing Critical-Sized Bone Defects

Large segmental defects of load-bearing long bones remain among the most complex reconstructive problems in orthopedic surgery. These injuries arise in the context of tumor resection, high-energy trauma, infection, and revision procedures, and they frequently exceed the intrinsic regenerative capacity of bone. A defect is considered critical sized when spontaneous healing cannot be expected to occur during the lifetime of the host without surgical intervention [1, 2]. Successful reconstruction must therefore achieve two simultaneous objectives: immediate structural stability sufficient to permit weight bearing, and a biological environment conducive to long-term osseous regeneration.

Current treatment strategies include autografts, allografts, vascularized bone transfer, distraction osteogenesis, and metallic endoprostheses, each carrying distinct limitations. Autografts, bone harvested from a secondary surgical site within the same patient, are considered the gold standard for managing bone defects owing to their unique combination of osteoconductivity, osteoinductive growth factors, and viable osteogenic cells, properties that no synthetic substitute can fully replicate. However, autografts harvest introduces donor site morbidity, including chronic pain, sensory disturbance, and risk of fracture, and the harvestable volume is fundamentally limited, making autograft impractical for reconstruction of large segmental defects constraining their clinical applicability [3]. Allografts are bone sourced from cadaveric donors and processed offering an alternative that avoid donor site morbidity and supply constraints. They are widely used in revision surgery and tumor reconstruction where defect size exceeds what autograft can fill [4]. However, allograft processing, which typically involves demineralization, freeze-drying, or irradiation to reduce immunogenicity and disease transmission risk, substantially diminishes osteoinductive potential and mechanical integrity. Structural allografts consequently carry elevated risks of fracture, nonunion, and immune mediated failure, and their long-term incorporation into host bone

is inconsistent [4]. Xenografts, a bone derived materials sourced from non-human species, most commonly bovine represent a third class of biological graft material. Deproteinized bovine bone mineral (DBBM) and acellular bone matrix (ABM) products derived from bovine cortical and cancellous bone have been extensively characterized, are FDA approved, and are commercially available in numerous forms including granules, blocks, and putties [28, 29]. Their highly osteoconductive mineral phase supports cell attachment and new bone deposition, and their established safety and regulatory status have led to widespread clinical adoption in craniofacial, periodontal, and orthopedic applications[28]. Despite these advantages, commercially available xenograft products are supplied as passive void fillers rather than architecturally engineered constructs. They lack the geometric precision, interconnected porosity, and mechanical predictability necessary for load-bearing long-bone reconstruction, and their degradation behavior and mechanical properties cannot be systematically tuned to match defect specific requirements. It is precisely this limitation that creates a gap between the excellent biological properties of ABM-derived mineral and the architectural and mechanical inadequacy of its current clinical forms , that motivates the engineering of patient-specific TPMS scaffolds fabricated from deproteinized bone mineral. Metallic endoprostheses restore immediate mechanical function but are biologically inert structures that do not remodel with the host skeleton and may generate pathological stress shielding that compromises long-term implant survival [5]. None of these strategies reliably restores functional bone in large defects while avoiding the complications inherent to each approach.

Bone tissue engineering (BTE) has emerged as an alternative paradigm, aiming to regenerate functional bone within large defects using biomaterial scaffolds designed to guide cellular infiltration, vascularization, and osteogenesis [6,7]. However, large segmental defects in load-bearing long bones impose an additional and competing set of demands: the scaffold must simultaneously withstand the cyclic physiologic forces transmitted through the limb during the healing period, before sufficient bone ingrowth has occurred to share the mechanical burden. This coupling of structural and biological requirements where increasing porosity to support regeneration directly reduces the mechanical integrity needed to survive loading is the central and unresolved design

challenge for load-bearing BTE scaffolds. The following sections outline these requirements and identify the gaps in understanding that motivate the present work.

1.2 Mechanical Requirements of Bone Tissue Engineering Scaffolds

Scaffolds intended for critical-sized defects in load-bearing bones must simultaneously satisfy a set of design constraints that are, in several respects, mutually antagonistic. They must provide sufficient mechanical integrity to sustain physiologic loading without failure, while also exhibiting the high porosity and pore interconnectivity necessary to permit vascular ingrowth, cellular migration, and nutrient transport. They must provide surface bioactivity to support osteoconduction, osteoinduction and osseointegration, properties that are intrinsic to calcium phosphate ceramics and represent their primary biological advantage over metallic and polymeric alternatives[19]. They must degrade at a rate compatible with the progression of bone regeneration, ensuring that mechanical load is progressively transferred to the newly formed bone.

The central tension in scaffold design is the inverse relationship between porosity and structural strength. Increasing porosity enhances biological performance by providing greater surface area for cell attachment and more permissive channels for tissue infiltration, but it reduces the solid material available to bear load. Increasing density recovers structural capacity but limits cellular migration and vascularization, ultimately impairing regeneration. Achieving an optimal balance between these competing requirements remains a central and unresolved challenge in scaffold engineering.

Of critical importance to load-bearing scaffold design is the recognition that neither structural integrity nor biological function alone defines success but it is the simultaneous achievement of both that determines whether a scaffold performs as intended in vivo. Bone regeneration is highly sensitive to the local mechanical environment, including strain magnitude, stress distribution, and fluid shear stress acting on resident and infiltrating cells [8,9,10]. A scaffold that is structurally adequate at the macroscale may nonetheless fail biologically if its internal architecture generates a mechanical microenvironment incompatible with osteogenesis. Scaffold architecture must therefore be evaluated not only for structural robustness but also for its capacity to establish

the mechanobiological conditions necessary for successful regeneration.

1.3 Mechanical Regulation of Bone Regeneration

Bone is a mechanosensitive tissue whose regenerative response is profoundly shaped by local mechanical stimuli. Foundational mechanoregulation models proposed that tissue differentiation at a healing site is governed by the combined effects established quantitative frameworks for predicting tissue differentiation outcomes based on the local mechanical environment at a healing site. Carter and colleagues proposed that the combination of cyclic stress history and hydrostatic stress governs the tissue phenotype that emerges during repair, with compressive hydrostatic stress and low deviatoric strain favoring direct bone formation, and tensile or high shear strain environments promoting fibrous tissue instead [8]. Claes and Heigele subsequently refined this framework by defining specific strain magnitude thresholds along the periosteal surface of healing fractures: interfragmentary strains below approximately 5% in combination with moderate compressive hydrostatic stress were associated with intramembranous ossification i.e. the direct deposition of woven bone without a cartilaginous intermediate; while strains in the range of 5–15% combined with hydrostatic compression promoted endochondral ossification, in which a cartilage template is first formed and subsequently mineralized [9]. Strains exceeding approximately 15%, particularly when accompanied by tensile or shear loading, were associated with fibrous connective tissue formation and impaired union [9]. This strain-dependent bifurcation of the ossification pathway has direct implications for scaffold design: a mechanical environment that maintains interfragmentary or intrascaffold strain below 5% under physiologic loading is necessary to bias tissue differentiation toward the intramembranous pathway and achieve the rapid, direct bone formation that is most desirable in a load-bearing critical defect.

Subsequent biophysical frameworks further refined this understanding by incorporating the role of interstitial fluid flow alongside solid-phase deformation. Prendergast and colleagues proposed that mechanobiological outcomes at the cell scale are governed by the coupled influence of shear strain in the solid matrix and fluid velocity in the pore space, with distinct combinations of these stimuli

predicting bone, cartilage, or fibrous tissue differentiation [10]. This fluid-solid coupling is particularly relevant for highly porous scaffolds, where the interconnected pore network sustains significant interstitial flow under dynamic loading and where fluid shear stress acting on adherent cells may amplify or modify the solid-phase strain stimulus. These models have been corroborated by experimental work demonstrating that strain magnitudes in the range of approximately 100–3,000$\mu\varepsilon$ promote osteogenic differentiation in bone cells and are associated with adaptive bone formation in intact cortical bone [11, 13], while strain magnitudes below approximately 100$\mu\varepsilon$ fall below the threshold for mechanotransductive activation and may result in disuse mediated resorption [13]. Strain magnitudes exceeding approximately 10,000–15,000$\mu\varepsilon$ are associated with microdamage accumulation and pathological remodeling [13]. The osteogenic window, roughly 100–3,000$\mu\varepsilon$ under cyclic physiologic loading, therefore represents the target mechanical environment that scaffold design and external modulation strategies in the present work aim to achieve and preserve.

In vivo strain measurements in intact long bones during normal ambulation indicate that physiologic axial strains are maintained within a relatively narrow window [13, 14]. Successful defect repair requires that the mechanical environment within the regenerating tissue remains within this osteogenic range throughout the healing period. Excessive interfragmentary strain magnitudes exceeding approximately 15% impair direct bone formation and redirect tissue differentiation toward fibrocartilage or fibrous tissue, consistent with the strain-dependent ossification thresholds described above [9]. Conversely, strain magnitudes falling below the mechanotransductive activation threshold of approximately 100$\mu\varepsilon$, may occur under prolonged mechanical unloading or aggressive stress shielding by fixation hardware which removes the cyclic stimulus necessary to sustain osteoblast activity and guide progressive bone deposition, potentially resulting in disuse-mediated resorption rather than regeneration [13].

For scaffolds implanted within large segmental defects, the internal strain environment is determined by the interaction of multiple factors: the architectural geometry of the scaffold, the elastic properties of the constituent material, the design of the fixation construct, and the load-

sharing behavior between the implant and the host bone. Despite extensive efforts to develop new scaffold architectures and materials, the internal strain state within porous ceramic scaffolds under clinically relevant fixation conditions remains insufficiently characterized. This gap between bulk mechanical testing and *in situ* deformation behavior represents a significant obstacle to rational scaffold optimization.

1.4 Influence of Fixation Constructs on Defect Mechanics

In clinical practice, large, long-bone defects are stabilized using locking compression plates or intramedullary fixation devices that bridge the defect and restore structural continuity. These constructs fundamentally alter the mechanical environment experienced by the scaffold [9, 12]. Mechanical forces are not transmitted directly through the scaffold in isolation; instead, they are distributed through the host bone and fixation hardware before reaching the defect region.[33, 34] The scaffold therefore exists within a mechanically complex system in which the magnitude, direction, and distribution of forces acting on it are substantially modified by the fixation construct. Experimental investigations of plated segmental defect models have demonstrated that metallic fixation hardware assumes a substantial proportion of the applied load, shielding the defect region from direct mechanical loading. Stoffel et al. reported that locking compression plate constructs carry approximately 70–90% of the applied axial force depending on plate stiffness and working length, meaning the scaffold within the defect gap experiences a substantially reduced and mechanically altered load relative to the externally applied force[15]. This load partitioning has important implications for scaffold design that are not captured by conventional axial compression testing. We hypothesize that when fixation hardware dominates load transfer, bulk compressive strength may not be the primary determinant of scaffold survival or biological performance. Rather, we propose that the local strain distribution within the scaffold including the transverse deformations and bending modes that arise from the complex loading transmitted through the construct, becomes the more clinically relevant parameter. Scaffold failure under these conditions

may be governed by localized bending or transverse tensile strain rather than axial compressive overload. Understanding how physiologic loading is transferred through plated constructs into porous scaffolds is therefore essential for rational scaffold design is one primary contribution of the present work.

1.5 Architectural Control Using Triply Periodic Minimal Surfaces

Advances in additive manufacturing have enabled the precise fabrication of complex porous architectures from ceramic materials, including triply periodic minimal surface (TPMS) geometries [11, 16, 32]. TPMS structures are defined by mathematically continuous surfaces with zero mean curvature at every point, producing fully interconnected pore networks with smooth, continuous solid walls [16, 17]. These geometric properties address several limitations of conventional stochastic or rectilinear porous architectures. The smooth internal surfaces of TPMS scaffolds reduce local stress concentrations relative to sharp-edged lattice geometries, while the fully interconnected porosity ensures unobstructed pathways for vascular and cellular infiltration throughout the scaffold volume. The surface area-to-volume ratio and nominal porosity of TPMS structures can be tuned systematically by adjusting the unit cell scale and surface, enabling controlled variation of architectural parameters independently of material composition.

Among available TPMS topologies, Gyroid structures have been the most extensively studied in bone tissue engineering. However, other TPMS geometries including the Fischer–Koch S (FKS), Schwarz P, and Diamond surfaces exhibit distinct mechanical behaviors arising from differences in their surface topology and internal load path geometry [18]. Finite element homogenization analyses have demonstrated that TPMS scaffolds possess cubic elastic symmetry with anisotropic elastic constants that are sensitive to porosity, and that these anisotropic properties differ systematically across topologies [18]. This topology dependent anisotropy may have direct implications for how strain is distributed within a scaffold subjected to the multiaxial loading conditions that prevail under clinical fixation.

Despite growing interest in TPMS scaffolds, comparative evaluation of alternative TPMS

topologies under clinically relevant mechanical conditions remains limited. Most studies have been conducted computationally or analytically. Most comparative studies have characterized mechanical properties under idealized uniaxial compression, without considering how architectural differences influence strain redistribution when fixation hardware modulates the applied loading. Understanding whether topology selection influences the strain microenvironment within a plate-stabilized defect is necessary to guide rational scaffold design for load-bearing applications.

1.6 Limitations of Internal Reinforcement Strategies

Hydroxyapatite and other calcium phosphate ceramics are well established scaffold materials owing to their compositional similarity to native bone mineral and their strong osteoconductive properties, which promote direct attachment and migration of osteogenic cells along ceramic surfaces [19]. However, these materials are inherently brittle and susceptible to fracture when subjected to bending or transverse tensile loading, failure modes that are particularly relevant under the complex strain conditions generated within a fixation construct.

Conventional strategies to improve ceramic scaffold toughness involve composite reinforcement through polymer infiltration or fiber incorporation. While these approaches can enhance fracture resistance, they introduce significant trade-offs. Polymer infiltration reduces both the surface area available for osteogenic cell attachment and pore interconnectivity which alter the degradation kinetics of both the ceramic and polymer phases. Fiber reinforcement can compromise the homogeneity of the pore network and introduce heterogeneous material interfaces that may generate stress concentrations or provoke adverse biological responses. These trade-offs raise legitimate concerns about whether internal composite reinforcement can be achieved without compromising the osteoconductive surface chemistry and pore architecture that motivate the use of calcium phosphate ceramics in the first place.

An alternative approach is external mechanical modulation: modifying the strain environment experienced by the scaffold through an external constraint, rather than altering its composition. If a compliant external element such as a polymer sleeve placed around the scaffold perimeter could

selectively reduce the transverse deformations that predispose ceramic scaffolds to brittle fracture, it might be possible to improve mechanical compatibility without compromising scaffold porosity, surface bioactivity, or degradation behavior. This hypothesis motivates the endoprosthetic sleeve design explored in the present work.

1.7 Need for Experimental Strain Quantification

Although computational studies have modeled stress distributions and fluid flow within idealized porous scaffold geometries [20], experimental measurement of scaffold strain within the clinically representative construct configuration of a porous scaffold seated within a segmental long-bone defect stabilized by a locking compression plate and subjected to physiologic compressive loading remains sparse. Most of the scaffold mechanical characterization relies on bulk uniaxial compression testing conducted in isolation from the fixation hardware and host bone that would be present in clinical use [35, 36]. This approach may significantly misrepresent the strain state experienced by a scaffold *in vivo*, where load sharing by the fixation construct reduces axial demand while potentially amplifying transverse and bending deformations.

Direct quantification of both axial and transverse strain under physiologically representative loading conditions is necessary to determine whether internal strain falls within osteogenic thresholds, to identify the deformation modes most likely to govern scaffold mechanical failure, and to establish whether architectural differences between TPMS topologies produce measurable differences in strain transfer. Such data also provides the empirical basis required to calibrate and validate computational models, without which finite element predictions remain insufficiently grounded in experimental reality. The absence of this experimental foundation has constrained scaffold optimization to bulk property comparisons that may not reflect clinically relevant performance, which is addressed in with this work.

1.8 Role of Finite Element Modeling in Scaffold Optimization

Finite element analysis provides a powerful complement to experimental investigation by enabling

prediction of internal stress and strain fields that are inaccessible to direct measurement in porous scaffold geometries. Microstructural modeling approaches can resolve how scaffold architecture, material stiffness, and boundary conditions interact to govern local deformation and flow behavior, and they enable parametric evaluation of design modifications that would be impractical to implement experimentally at scale [20]. These capabilities are particularly valuable for evaluating sleeve geometry variations, where the design space is large and the interactions between sleeve stiffness, contact mechanics, and scaffold strain redistribution are complex.

However, the predictive value of finite element models depends critically on their validation against experimental data. A computational model that reproduces experimentally measured strain distributions under known loading conditions can be used with confidence to explore conditions that are difficult to instrument directly, such as internal stress gradients within scaffold strut walls or strain concentrations at the scaffold-bone interface that surface mounted gauges cannot resolve.

The integration of experimental strain measurements with finite element modeling in this work is underpinned by a constitutive mapping framework that relates measurements made on PLA polymer scaffolds to the expected mechanical response of equivalent ceramic constructs. This mapping is justified on two theoretical grounds. First, both PLA and the ovine bone mineral ceramic behave as linearly elastic solids within the applied strain range of less than 2% nominal deformation, meaning that stress and strain are related through fixed stiffness and compliance matrices that can be determined experimentally and applied as linear transformations[37]. Second, the Gyroid architecture imposes effective cubic elastic symmetry at the macroscopic scale regardless of the intrinsic anisotropy of the printed polymer, because the threefold rotational symmetry of the TPMS unit cell constrains the homogenized elastic response to follow cubic symmetry relationships with only three independent elastic constants[38]. This architectural isotropy means that the scaffold's effective mechanical behavior is governed by its topology rather than the printing direction of the constituent material, justifying the use of isotropic stiffness and compliance matrices in the constitutive transformation and supporting the validity of mapping experimentally measured PLA strain states to ceramic-equivalent values under identical external loading conditions.

The experimental strain measurements reported in this dissertation therefore serve a dual purpose, they directly characterize the mechanical environment within the scaffold-bone construct under physiologic loading, and they provide the empirical validation dataset against which finite element predictions are compared. It also establishes ground truth, models extend predictions beyond what experiments can measure, and iterative comparison between the two supports progressive refinement of both the model and the scaffold design. This combined approach is the methodological foundation of the present dissertation.

1.9 Central Hypothesis

The central hypothesis of this dissertation is that, in load-bearing critical sized long-bone defects stabilized with locking plate constructs, the mechanical survival and osteogenic potential of a porous ceramic scaffold are is governed primarily by the internal strain environment rather than bulk compressive strength, and that external mechanical modulation through a compliant endoprosthetic sleeve can reduce deleterious transverse strain while preserving the physiologic axial compressive loading necessary to support osteogenesis. This reframing shifts the design objective from maximizing scaffold strength in isolation to engineering the strain microenvironment that the scaffold presents to regenerating tissue under clinically realistic loading conditions.

1.10 Specific Aims

To test this hypothesis, the following specific aims were established:

Aim 1. Evaluate and compare the permeability and mechanical performance of two TPMS scaffold architectures, Gyroid and Fischer–Koch S, fabricated at equivalent nominal porosity, and quantify the magnitude of topology dependent differences in Darcian permeability, compressive strength, elastic modulus, and failure behavior. The goal was to determine whether architectural topology produces measurable and clinically meaningful differences in the balance between fluid transport and structural performance, assessed against the permeability and mechanical property ranges reported for native cancellous bone.

Aim 2. Experimentally quantify both axial and transverse principal strain within porous ceramic scaffolds under physiologic compressive loading in a plate-stabilized ovine metatarsal segmental defect model, establishing the multiaxial mechanical environment experienced by the scaffold under clinically representative fixation and loading conditions.

Aim 3. Design and fabricate a polycaprolactone endoprosthetic sleeve, a low stiffness external enclosure positioned around the scaffold perimeter and assess its capacity to selectively reduce transverse strain within the scaffold without altering scaffold composition, porosity, or surface chemistry, and without attenuating the axial compressive strain necessary for osteogenesis.

Aim 4. Construct and experimentally validate finite element models capable of predicting the strain distribution within scaffold–bone–sleeve constructs and use the validated models to establish a parametric computational framework for evaluating the influence of sleeve geometry on internal strain redistribution.

1.11 Bibliography

1. G. I. Taylor et al., "Defining critical size in bone defect healing," Clin. Orthop. Relat. Res., vol. 473, pp. 2898–2904, 2015.

2. R. Dimitriou, E. Jones, D. McGonagle, and P. V. Giannoudis, "Bone regeneration: current concepts and future directions," BMC Med., vol. 9, p. 66, 2011.

3. J. Younger and M. Chapman, "Morbidity at bone graft donor sites," J. Orthop. Trauma, vol. 3, pp. 192–195, 1989.

4. A. Delloye et al., "Bone allografts: What they can offer and what they cannot," J. Bone Joint Surg. Br., vol. 89, pp. 574–580, 2007.

5. S. Takizawa et al., "Stress shielding and bone remodeling," Acta Biomater., vol. 63, pp. 1–12, 2018.

6. R. Langer and J. Vacanti, "Tissue engineering," Science, vol. 260, pp. 920–926, 1993.

7. B.-N. B. Nguyen et al., "Dynamic Bioreactor Culture of High Volume Engineered Bone Tissue," Tissue Eng. Part A, vol. 22, pp. 263–271, 2016.

8. D. R. Carter et al., "Mechanobiology of skeletal regeneration," Clin. Orthop., vol. 227, pp. 239–255, 1988.

9. L. Claes and C. Heigele, "Magnitudes of local stress and strain predict tissue differentiation,"J. Biomech., vol. 32, pp. 255–266, 1999.

10. P. J. Prendergast et al., "Biophysical stimuli at implant interfaces," J. Biomech., vol. 30, pp. 539–548, 1997.

11. U. Meyer et al., "Mechanical stimulation and osteogenesis," J. Biomech., vol. 39, pp. 2727–2736, 2006.

12. S. Perren, "Physical and biological aspects of fracture healing," Injury, vol. 33, pp. 3–10, 2002.

13. L. Lanyon, "Functional strain in bone," J. Biomech., vol. 17, pp. 897–905, 1984.

14. A. Hoshaw et al., "In vivo measurement of bone strain," J. Biomech., vol. 30, pp. 341–349, 1997.

15. K. Stoffel, U. Dieter, G. Stachowiak, A. Gächter, and M. S. Kuster, "Biomechanical testing of the LCP — how can stability in locked internal fixators be controlled?," Injury, vol. 34, suppl. 2, pp. SB63–SB69, 2003.

16. S. Melchels et al., "Additive manufacturing of TPMS scaffolds," Biomaterials, vol. 31, pp. 6909–6916, 2010.

17. I. Maskery et al., "Mechanical properties of TPMS structures," Acta Mater., vol. 152, pp. 62–71, 2018.

18. Y. Lu et al., "Anisotropic elastic behavior of TPMS-based scaffolds," J. Mech. Behav. Biomed. Mater., vol. 99, pp. 56–65, 2019.

19. J. Dorozhkin, "Calcium orthophosphate-based bioceramics," Materials, vol. 2, pp. 399–498, 2009.

20. C. Sandino et al., "Finite element study of mechanical stimuli in scaffolds," J. Biomech., vol. 41, pp. 1005–1014, 2008.

21. B.-N. B. Nguyen, H. Ko, R. A. Moriarty, J. M. Etheridge, and J. P. Fisher, "Dynamic Bioreactor Culture of High Volume Engineered Bone Tissue," Tissue Engineering Part A, vol. 22, no. 3–4, pp. 263–271, Feb. 2016, doi: 10.1089/ten.tea.2015.0395.

22. M. Panagiotis, "Classification of Non-Union," Injury, vol. 36, Suppl. 4, pp. S30–S37, 2005, doi: 10.1016/j.injury.2005.10.008

23. R. Burge, B. Dawson-Hughes, D. H. Solomon, J. B. Wong, A. King, and A. Tosteson, "Inci-dence and Economic Burden of Osteoporosis-Related Fractures in the United States, 2005–2025," Journal of Bone and Mineral Research, vol. 22, no. 3, pp. 465–475, Mar. 2007, doi: 10.1359/jbmr.061113.

24. L. Vidal, C. Kampleitner, M. Á. Brennan, A. Hoornaert, and P. Layrolle, "Reconstruction of Large Skeletal Defects: Current Clinical Therapeutic Strategies and Future Directions Using 3D Printing," Frontiers in Bioengineering and Biotechnology, vol. 8, Art. 61, 2020, doi: 10.3389/fbioe.2020.00061.

25. H. Bezstarosti et al., "Management of Critical-Sized Bone Defects in the Treatment of Fracture-Related Infection: A Systematic Review and Pooled Analysis," Archives of Orthopaedic and Trauma Surgery, vol. 141, no. 7, pp. 1215–1230, 2021, doi: 10.1007/s00402-020-03525-0.

26. D. J. Hak et al., "Delayed Union and Nonunions: Epidemiology, Clinical Issues, and Financial Aspects," Injury, vol. 45, Suppl. 2, pp. S3–S7, 2014, doi: 10.1016/j.injury.2014.04.002.

27. J. Henkel et al., "Bone Regeneration Based on Tissue Engineering Conceptions – A 21st Century Perspective," Bone Research, vol. 1, no. 3, pp. 216–248, 2013, doi: 10.4248/BR201303002.

28. Geiger et al. (2003) on DBBM clinical performance — European Spine Journal, 12(Suppl 2), S106–S117

29. Oryan et al. (2014) for a broad review of bone graft substitutes including xenografts — Journal of Orthopaedic Science, 19(1), 1–18

30. M. Govoni et al., "Commercial Bone Grafts Claimed as an Alternative to Autografts: Current Trends for Clinical Applications in Orthopaedics," *Materials*, vol. 14, no. 12, Art. 3290, 2021, doi: 10.3390/ma14123290.

31. P. V. Giannoudis, T. A. Einhorn, and D. Marsh, "Fracture Healing: The Diamond Concept,"*Injury*, vol. 38, Suppl. 4, pp. S3–S6, 2007, doi: 10.1016/S0020-1383(08)70003-2.

32. S. Bose, D. Ke, H. Sahasrabudhe, and A. Bandyopadhyay, "Additive Manufacturing of Biomaterials," *Progress in Materials Science*, vol. 93, pp. 45–111, 2018, doi: 10.1016/j.pmatsci.2017.08.003.

33. K. Stoffel, U. Dieter, G. Stachowiak, A. Gächter, and M. S. Kuster, "Biomechanical testing of the LCP — how can stability in locked internal fixators be controlled?," *Injury*, vol. 34, suppl. 2, pp. SB63–SB69, 2003.

34. G. N. Duda et al., "Influence of muscle forces on femoral strain distribution," *Journal of Orthopaedic Research*, vol. 20, no. 6, pp. 1354–1361, 2002.

35. V. Karageorgiou and D. Kaplan, "Porosity of 3D biomaterial scaffolds and osteogenesis,"*Biomaterials*, vol. 26, no. 27, pp. 5474–5491, 2005, doi: 10.1016/j.biomaterials.2005.02.002.

36. K. Rezwan, Q. Z. Chen, J. J. Blaker, and A. R. Boccaccini, "Biodegradable and bioactive

porous polymer/inorganic composite scaffolds for bone tissue engineering," *Biomaterials*, vol. 27, no. 18, pp. 3413–3431, 2006, doi: 10.1016/j.biomaterials.2005.01.078.

37. R. A. Cláudio, J. Dupont, R. Baptista, M. Leite, and L. Reis, “Behaviour evaluation of 3D printed polylactic acid under compression,” *Journal of Materials Research and Technology*, vol. 21, pp. 4052–4066, Nov. 2022, doi: 10.1016/j.jmrt.2022.10.042.

38. Y. Lu, W. Zhao, Z. Cui, H. Zhu, and C. Wu, "The anisotropic elastic behavior of the widely-used triply-periodic minimal surface based scaffolds," Journal of the Mechanical Behavior of Biomedical Materials, vol. 99, pp. 227–239, 2019, doi: 10.1016/j.jmbbm.2019.07.018.

Chapter 2

Comparing Fischer–Koch S and Gyroid Hydroxyapatite Scaffolds: Experimental Evaluation of Darcian Permeability

2.1 Introduction

Successful regeneration of critically sized bone defects requires the restoration of biological mass transport within the defect site. The permeability of a porous scaffold governs the movement of interstitial fluid through the pore network, and thereby mediates the nutrient and oxygen delivery, metabolic waste removal, and the generation of fluid shear stresses that drive mechanotransductive signaling at the cell surface mechanotransductive signaling [10]. These transport mechanisms directly influence osteogenic differentiation, angiogenesis, and vascular infiltration essential prerequisites for long-term integration of engineered constructs [1, 2].

At the macroscale, fluid movement through a porous scaffold is characterized by Darcy's law, which relates the superficial velocity of a viscous fluid to the pressure gradient across the medium through a material constant known as the Darcian permeability. The validity of this linear relationship is contingent upon laminar, creeping flow conditions, typically quantified by a Reynolds number below one (Re <1). At this regime, viscous forces dominate and inertial contributions to flow resistance are negligible [2, 3]. At higher flow rates, even within geometrically regular pore networks, inertial effects become non-trivial, and the linear Darcy relationship underestimates total flow resistance. Under these conditions, the Forchheimer extension of Darcy's law is employed, which introduces a quadratic velocity term to account for the additional pressure losses attributable to inertial momentum changes within the pore space [3, 4]:

$$\Delta P/L = (\mu/k_1)v + (\rho/k_2)v^2 \quad (2.1)$$

where $\Delta P/L$ is the pressure drop per unit length (Pa/m), μ is the dynamic viscosity of the fluid (Pa·s),

v is the superficial velocity (m/s), ρ is the fluid density (kg/m3), k_1 is the Darcian (viscous) permeability constant (m^2), and k_2 is the non-Darcian (inertial) permeability constant (m). In scaffold systems relevant to tissue engineering, flow rates are typically maintained well within the Darcian regime, so the second term becomes negligible, and permeability reduces to its classic single-parameter Darcian form [3].

The biological significance of permeability extends beyond simple nutrient delivery. Vossenberg et al. [3] demonstrated computationally that the Darcian permeability constant k is a reliable predictor of wall shear stress in regular printed scaffold systems for tissue engineering. Their work, using computational fluid dynamics (CFD) simulations on scaffolds with perpendicular fiber architectures, showed that shear stress acting on scaffold fibers decreases monotonically with increasing k, and that below a critical k value of approximately 1×10^{-10} m^2, small changes in scaffold dimensions such as those introduced by cell growth and extracellular matrix deposition can produce significant increases in shear stress that may impair cell attachment and proliferation. This finding underscores that permeability is not merely a transport parameter but a design variable with direct implications for cellular mechanobiology in perfusion bioreactor systems.

Computational approaches to predicting scaffold permeability include mathematical modelling, multiscale methods, and CFD simulations. Syahrom et al. [5] conducted a comprehensive CFD based permeability study on both natural and idealized cancellous bone structures, demonstrating that permeability increases linearly with porosity and decreases linearly with bone surface area. Their study showed that natural cancellous bone exhibits permeability values spanning from 2.56×10^{-11} m^2 to 7.43×10^{-8} m^2, with structural orientation markedly influencing transport behavior. These findings are directly relevant to scaffold design: structures with equivalent porosity but different surface area like the distinct TPMS topologies may exhibit substantially different permeability characteristics.

Native vertebral cancellous bone exhibits permeability values on the order of 10^{-8} m^2, which

provides the primary biological reference target for scaffold evaluation [6]. It is important to recognize, however, that bone permeability is hierarchical and scale dependent. At the lacunar–canalicular system (LCS) level the microscale pore network surrounding osteocytes, Gardinier et al. [7] experimentally measured a Darcian permeability of $2.8 \pm 1.8 \times 10^{-23}$ m^2 using rapid compression of intact canine metacarpals and intramedullary pressure recordings. This value, several orders of magnitude lower than macroscale cancellous permeability, highlights that bone fluid transport operates across multiple distinct porosity levels. For bone tissue engineering scaffolds targeting macroscale nutrient delivery and vascular infiltration, the relevant benchmark remains the cancellous bone permeability range (~10^{-9} to 10^{-8} m^2) rather than the LCS level.

Triply periodic minimal surface (TPMS) architectures have emerged as particularly promising scaffold geometries due to their continuous internal porosity, zero mean curvature, and mathematically scalable unit cell topology. These properties confer a favorable combination of high surface-area-to-volume ratio and well connected pore networks, both promote cell attachment and fluid perfusion [11, 12]. Computational and experimental investigations consistently demonstrate that permeability in TPMS structures is governed principally by porosity, pore size distribution, and tortuosity [1, 5]. The smooth curvature of TPMS surfaces also minimizes stress concentrations that could promote cracking in ceramic materials, conferring structural advantages relative to conventional lattice strut-lattice or stochastic porous geometries.

Among the TPMS topologies investigated for bone tissue engineering, the Gyroid surface has been the most extensively characterized and serves as the current benchmark geometry [4]. Its bicontinuous sheet-network architecture produces interconnected pore channels without any mean curvature discontinuities, and its permeability behavior under Darcian flow conditions has been well documented across a range of porosities and length scales [4, 5, 12]. A second TPMS topology, the Fischer–Koch S (FKS) surface, has attracted theoretical interest owing to its distinct channel morphology and potentially superior surface-area distribution relative to the Gyroid at equivalent porosity. However, experimental characterization of FKS scaffolds remains limited, and

no published study to date has directly compared the fluid transport behavior of FKS and Gyroid hydroxyapatite constructs under matched fabrication and testing conditions.

This gap in the experimental record is significant because permeability cannot be reliably inferred from topology alone. The sintering process introduces dimensional shrinkage and microstructural changes that alter effective pore geometry in ways that are difficult to predict analytically, and even small differences in post-sintering wall thickness or pore connectivity can produce measurable differences in transport behavior. The infrared spectroscopy based approach developed by Gascoin et al. [8] illustrates this challenge more broadly: they showed that peak width of a tracer signal through porous metallic media correlates linearly with Darcian permeability, yet even a 2% uncertainty in optical measurement translated to a 50% uncertainty in the derived permeability a reminder that characterizing transport properties demands rigorous and well-validated experimental methodology. Furthermore, because scaffold permeability must be optimized in conjunction with structural performance, direct experimental comparison between FKS and Gyroid architectures under matched conditions is essential to evaluate their relative suitability for load-bearing bone regeneration. The relationship between permeability and shear stress established by Vossenberg et al. [3] is particularly pertinent in this context: if the permeability of the FKS scaffold falls near or below a critical threshold, shear stresses on the scaffold surface may exceed biologically tolerable levels during perfusion bioreactor culture, even if macroscale transport rates appear adequate.

Two principal computational approaches have been used to model fluid transport through porous scaffold geometries. The Brinkman equation extends Darcy's law by incorporating a viscous shear term that accounts for momentum transfer at solid-fluid boundaries, making it applicable to porous media with significant boundary layer effects. Direct numerical solution of the Navier-Stokes equations, implemented through computational fluid dynamics, resolves the full three-dimensional flow field within the pore space geometry without simplifying continuum assumptions, and is therefore more sensitive to local architectural complexity [3, 5].

The objective of this study was therefore to experimentally quantify the Darcian permeability of hydroxyapatite FKS and Gyroid scaffolds fabricated to equivalent nominal porosity, and to correlate

the measured transport behavior with structural characterization data obtained by micro-computed tomography (μCT). By providing direct experimental comparison under matched fabrication and testing conditions, this chapter establishes the permeability baseline required to contextualize the mechanical and biological performance assessments reported in subsequent chapters.

2.2 Materials and Methods

2.2.1 Scaffold Fabrication and Structural Characterization

Hydroxyapatite TPMS scaffolds were fabricated as 10 mm cubic constructs with a target design porosity of 70%. The fabrication protocol employed viscous printing of hydroxyapatite paste followed by thermal debinding and sintering. The cubic geometry was selected to match the characteristic specimen dimensions commonly employed in both computational permeability studies [5] and experimental perfusion testing [4], facilitating meaningful comparison with the broader literature.

Following sintering, micro-computed tomography (μCT) was performed on all specimens to determine as-built structural parameters. Quantified metrics included as-sintered porosity, mean wall thickness, mean wall spacing, and specific surface area. These morphological indices analogous to the trabecular thickness (Tb.Th), trabecular separation (Tb.Sp), and bone surface density (BS/BV) used to characterise natural cancellous bone microarchitecture [5] provide a quantitative basis for linking topology-dependent structural differences to measured transport behaviour.

FKS scaffolds exhibited an as-sintered porosity of $74.00 \pm 0.31\%$, substantially exceeding the 70% design target. In contrast, Gyroid scaffolds decreased slightly to $68.49 \pm 1.18\%$, falling marginally below the design value. This divergence in sintering behaviour is attributed to topology-dependent differences in the spatial arrangement of material during thermal consolidation: the FKS surface geometry may create local conditions that favour greater material redistribution or shrinkage anisotropy during sintering. Wall thickness for Gyroid scaffolds closely matched the

extrusion width (0.413 ± 0.112 mm), while FKS scaffolds measured slightly thicker at 0.424 ±0.148 mm. Mean wall spacing was greater in FKS scaffolds (1.212 ± 0.295 mm) than in Gyroid scaffolds (1.039 ± 0.200 mm), consistent with the higher as-sintered porosity. Specific surface area was also marginally higher for FKS (5.796 ± 0.042 mm^{-1}) compared to Gyroid (5.514 ± 0.175mm^{-1}). Higher porosity accompanied by greater surface area parallels the findings of Syahrom et al. [5], who identified that structures with larger surface areas generate greater resistance to fluid flow, partially counteracting the permeability benefit of increased void fraction.

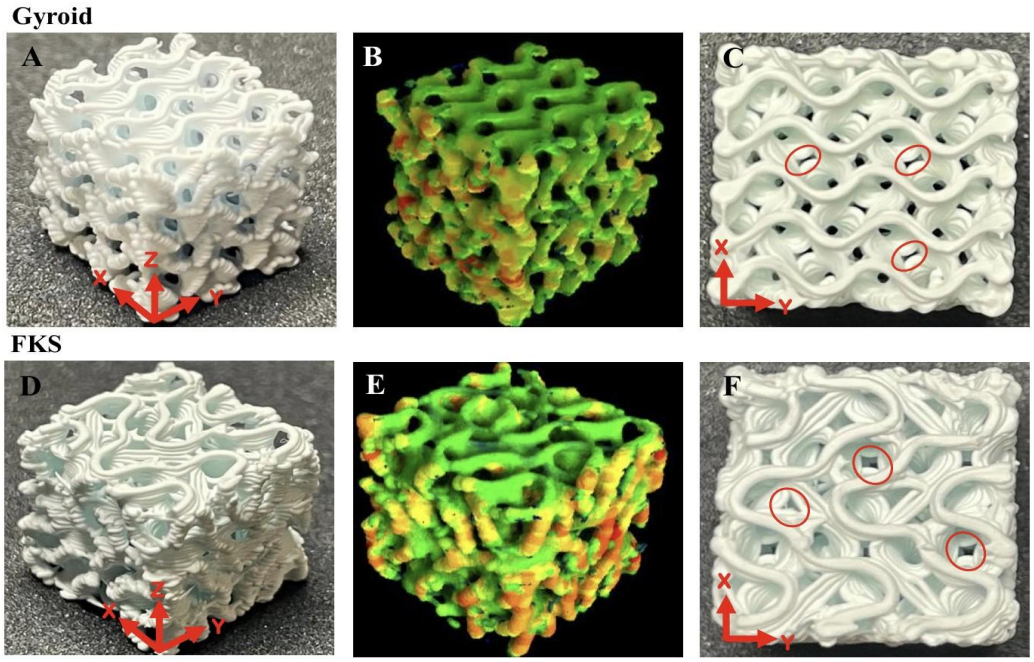

Figure 2.1: Representative images and micro-CT scans of 3D-printed and sintered cubic scaffolds. Column A/D shows isometric views of each topology (Gyroid: A–C; FKS: D–F). Column B/E displays 3D relative-thickness heatmaps from μCT data (red = thickest, green = thinnest). Column C/F shows top-view (x–y plane) slices; examples of layer gaps are circled.

These structural differences in particular the wider mean wall spacing and higher as-sintered porosity of FKS suggest topology-dependent variation in pore connectivity and tortuosity, which may in turn influence permeability. The coefficient of variation in wall thickness is notably higher for FKS (34.9%) than for Gyroid (27.1%), indicating greater structural heterogeneity within the

FKS architecture following sintering. This variability in local wall geometry may contribute to more irregular flow path distributions and, consequently, to the flow-rate sensitivity discussed in Section 2.4.

2.2.2 Permeability Measurement Apparatus and Protocol

Permeability was measured using a horizontal flow apparatus adapted from Santos et al. [4]. The experimental configuration closely mirrors the standard perfusion chamber approach widely adopted in cancellous bone permeability studies [5, 6], adapted for the specific geometry and mechanical fragility of sintered ceramic TPMS scaffolds. The system consisted of a 3D-printed test chamber housing the scaffold, a 100 mL glass syringe driven by a syringe pump at controlled volumetric flow rates, and a Validyne P17 differential pressure transducer connected across the scaffold to record the pressure drop. An elastomeric sleeve was fitted around each scaffold specimen prior to placement within the test chamber; this sleeve served to prevent bypass flow around the scaffold perimeter, ensuring that all fluid passed through the scaffold interior and that the measured pressure drop reflected the intrinsic scaffold resistance rather than a combination of scaffold and bypass pathways.

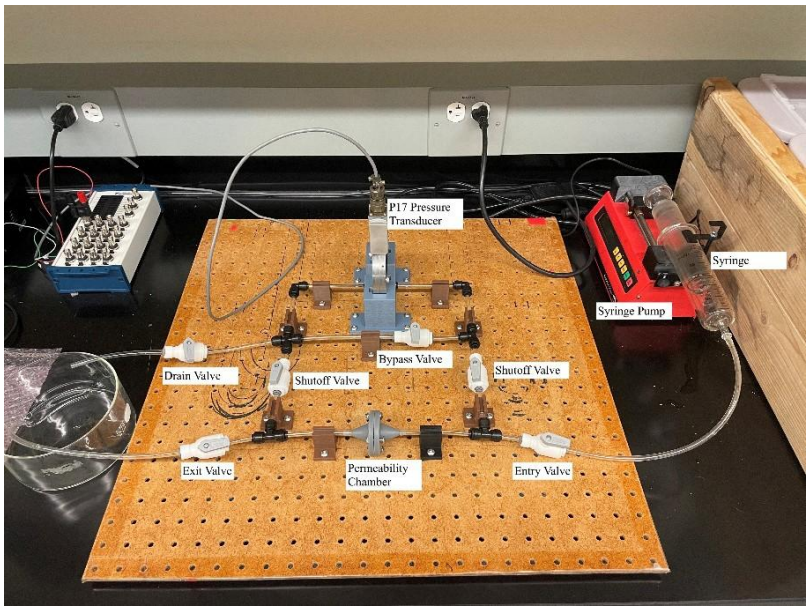

Figure 2.2: Schematic of the permeability measurement setup, showing the syringe pump, test chamber, scaffold specimen with elastomeric sleeve, differential pressure transducer, and data acquisition system

Flow rates of 1–5 mL/min were selected to replicate wall shear stress conditions relevant to osteoblastic differentiation in perfusion bioreactor systems. This range corresponds to superficial velocities that produce wall shear stresses within the physiologically relevant window for osteogenic stimulation, consistent with the framework established by Vossenberg et al. [3], who demonstrated that Darcian permeability directly governs the magnitude of shear stresses experienced by cells on scaffold fibres during perfusion culture. Flow rates were applied sequentially from lowest to highest, with each flow rate maintained until a stable pressure reading was obtained before recording commenced.

2.2.3 Fluid Properties and Darcian Validation

Laboratory temperature was maintained at 22.5°C throughout testing. Water was used as the perfusing fluid, consistent with the approach of numerous permeability studies on cancellous bone and porous scaffolds [5]. Water properties at 22.5°C were taken as: density ρ = 997 kg/m^3 and dynamic viscosity $\mu = 9.55 \times 10^{-4}$ Pa·s. The use of water at ambient temperature, rather than blood or marrow substitute at physiological temperature, is a standard simplification that enables controlled and reproducible testing; the intrinsic permeability k is a material property independent of fluid, so measured values are directly comparable across studies employing different fluids, provided Darcian conditions are satisfied [5].

To validate the Darcian assumption, the Reynolds number was calculated for each test condition according to:

$$Re = \rho v D / \mu \quad (2.2)$$

where v is the superficial (Darcy) velocity and D is a characteristic pore length scale. The maximum Reynolds number observed across all test conditions and both scaffold types was Re= 0.89, satisfying the criterion Re < 1 and thereby confirming that inertial contributions to the pressure drop were negligible throughout the experimental regime [2, 3]. Under these conditions, the Forchheimer equation (Eq. 2.1) reduces to its Darcian form, and the quadratic term associated with the non-Darcian permeability constant k_2 can be neglected. Darcian permeability was accordingly

determined by applying Darcy's law directly:

$$k = v\mu L / (\Delta P \cdot A) \quad (2.3)$$

where v is the superficial velocity (m/s), μ is the dynamic viscosity (Pa·s), L is the scaffold length in the flow direction (m), ΔP is the measured pressure drop across the scaffold (Pa), and A is its cross-sectional area (m^2). This is the standard form of Darcy's law applied to determine intrinsic scaffold permeability and is consistent with the formulation used across experimental permeability studies on both cancellous bone [5, 6] and TPMS scaffolds [4].

2.2.4 Pressure Transducer Calibration

Accurate permeability determination requires precise pressure measurement. The Validyne P17 differential pressure transducer (Validyne Engineering Corporation, California, USA) was calibrated prior to testing using a series of known static pressures applied via a water column of variable height. The calibration yielded a linear voltage-to-pressure relationship:

$$\text{Pressure (Pa)} = 260.8 \times \text{Volts} + 35.348 \quad (2.4)$$

with a coefficient of determination $R^2 = 0.9695$, indicating satisfactory linearity across the measurement range. The calibration procedure is directly analogous to the pressure transducer validation protocols described in classical permeability measurement frameworks [2]. The non-zero intercept (35.348 Pa) reflects a small systematic offset at zero differential pressure, which was accounted for in all subsequent permeability calculations by using the calibrated relationship rather than raw voltage output.

2.2.5 Experimental Design and Statistical Analysis

Five scaffolds per topology were tested in triplicate at each flow rate, yielding a total of fifteen independent pressure–velocity measurements per scaffold type at each flow rate. This sample size and replication strategy was designed to provide sufficient statistical power to detect modest permeability differences between topologies while also quantifying within-scaffold and between-scaffold variability.

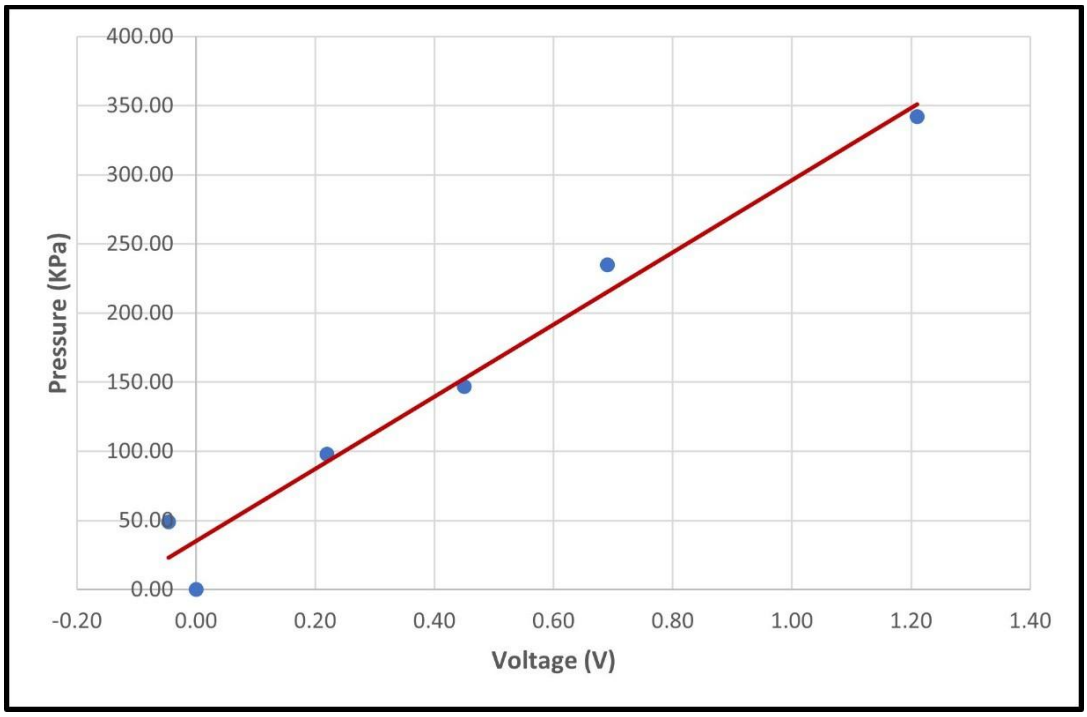

Figure 2.3: Pressure transducer calibration curve, showing measured pressure (Pa) as a function of transducer voltage output (V), with linear regression fit.

The linearity of pressure–velocity relationships was assessed visually and by linear regression for each scaffold at each flow rate, providing a graphical confirmation of Darcian behaviour. Pooled permeability values were calculated by averaging across all tested flow rates for each topology. Statistical comparisons were performed to evaluate differences between scaffold architectures, flow-rate dependence within each topology, and measurement repeatability between sessions. Paired t-tests were used for repeated measurements on the same specimens (i.e., first and second measurement sessions), enabling within-specimen comparison that controls for inter-specimen variability. One-way analysis of variance (ANOVA) was applied to assess differences in permeability across flow rates within each topology and between scaffold groups. Statistical significance was defined at $\alpha = 0.05$ throughout.

2.3 Results

2.3.1 Pressure–Velocity Linearity and Darcian Regime Confirmation

Linear pressure–velocity relationships were observed across all tested flow rates for both FKS and Gyroid architectures. Representative pressure–velocity plots for each topology demonstrated that the pressure drop scaled proportionally with superficial velocity throughout the 1–5 mL/min range, with high coefficients of determination ($R^2 > 0.98$ for all individual scaffold regressions). This linearity, combined with the verified Reynolds number ceiling of Re = 0.89, confirms that fluid transport through both TPMS architectures operated in the Darcian regime under all experimental conditions. No evidence of Forchheimer-type non-linearity which would manifest as a superlinear increase in pressure drop at higher flow rates was observed for either topology.

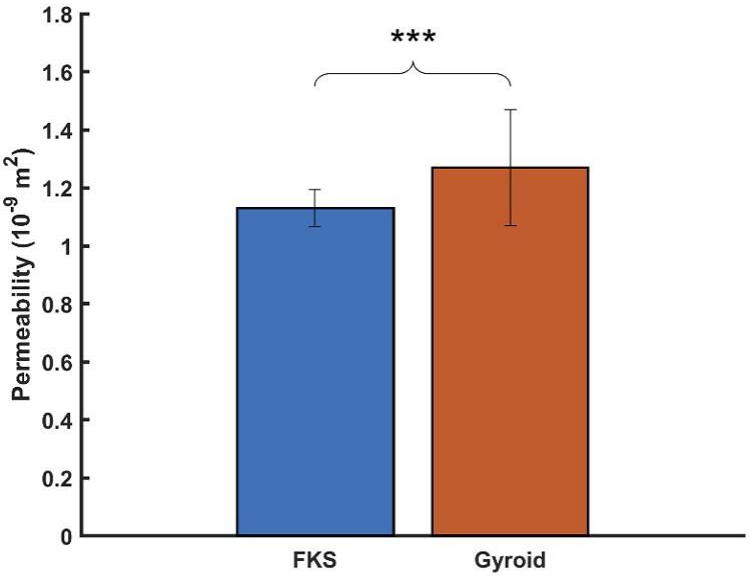

Figure 2.4: Mean Darcian permeability of Gyroid and FKS scaffolds across flow rates of 1–5 mL/min (n = 5 per group). Statistical significance is denoted by: *, P < 0.05; **, P < 0.01; ***, P < 0.001.

2.3.2 Measured Permeability Values

Average Darcian permeability values pooled across all flow rates were:

•FKS: $(1.13 \pm 0.06) \times 10^{-9}$ m^2

•Gyroid: $(1.27 \pm 0.20) \times 10^{-9}$ m^2

Gyroid scaffolds demonstrated approximately 11% greater mean permeability than FKS scaffolds. Both values fall within the 10^{-9} m^2 order of magnitude, consistent with reported permeability values for porous hydroxyapatite scaffolds [1, 4].

2.3.3 Flow-Rate Dependence

FKS scaffolds exhibited statistically significant flow-rate dependence in measured permeability (p = 0.016 for the first measurement set; p = 0.001 for the second), with a trend toward higher apparent permeability at elevated flow rates. Gyroid scaffolds exhibited no statistically significant flow-rate dependence (p = 0.341), with permeability values remaining essentially constant across the 1–5 mL/min range.

2.3.4 Between-Architecture Statistical Comparison

A paired t-test comparing FKS and Gyroid permeability across initial measurements yielded p = 0.055, indicating no significant difference at the α = 0.05 threshold. However, when scaffold-to-scaffold variability was accounted for using ANOVA, statistically significant differences between architectures emerged (p = 0.037 for the first measurement set; p = 0.006 for the second).

2.3.5 Measurement Repeatability

Repeatability testing between first and second measurement sessions for FKS scaffolds yielded p = 0.060, confirming no statistically significant intersession difference and supporting the experimental reliability of the permeability protocol. Similarly, Gyroid scaffolds showed

consistent permeability values between sessions. Had the sleeve been permitting peripheral leakage or mechanically deforming the scaffold between successive perfusion cycles, a systematic shift in measured permeability between the first and second sessions would be expected. The absence of any statistically significant intersession difference therefore supports both the sealing integrity of the sleeve and the conclusion that scaffold microstructure was not appreciably altered by successive perfusion under the applied flow conditions. The stability of repeated measurements validates the use of the elastomeric sleeve system to prevent bypass flow and confirms that scaffold microstructure was not appreciably altered by successive perfusion tests.

2.4 Discussion

2.4.1 Scaffold Permeability Relative to the Trabecular Bone Benchmark

Both FKS and Gyroid scaffold topologies produced permeability values on the order of 10^{-9} m^2, falling within the permeability ranges reported for other porous biomaterials used in bone tissue engineering [1, 4]. Syahrom et al. [5] compiled an extensive literature survey of experimental cancellous bone permeability values spanning from 2.56×10^{-11} m^2 to 7.43×10^{-8} m^2, depending on anatomical site, specimen orientation, and morphological indices; the present scaffolds fall comfortably within this range. The measured values confirm that neither FKS nor Gyroid architecture presents a fundamental barrier to nutrient transport or vascular infiltration at the tested porosity and across the range of flow rates applied in the present study.

However, the measured values remain approximately one order of magnitude below those reported for native vertebral cancellous bone (~10^{-8} m^2 [6]), indicating that further optimisation of pore geometry or porosity may be warranted if physiological permeability is a primary design target. In this context, the findings of Syahrom et al. [5] are instructive: their computational analyses showed that the prismatic plate-and-rod idealised structure most closely replicated natural cancellous bone permeability, and that the tetrakaidecahedral rod only structure achieved the

highest simulated permeability values (~5.34 × 10^{-8} m^2) by virtue of its predominantly open, interconnected strut architecture. TPMS topologies, by contrast, present closed sheet-like wall architectures that inherently impose greater viscous resistance than open-strut networks at equivalent bulk porosity. Increasing the nominal design porosity of TPMS scaffolds beyond 70% may improve alignment with the physiological benchmark, though this must be balanced against the attendant reduction in mechanical performance.

It is also instructive to consider permeability across different length scales of bone. Gardinier et al. [7] measured the LCS Darcian permeability of canine cortical bone to be 2.8 ± 1.8 × 10^{-23} m^2 fourteen orders of magnitude smaller than the macroscale permeability of the present scaffolds. This comparison underscores the hierarchical nature of bone fluid transport: the scaffold permeability values reported here are relevant to macroscale nutrient and oxygen supply, whereas LCS-level transport governs osteocyte mechanosensing and pericellular fluid shear [10]. Bone tissue engineering scaffolds operating at the macroscale cannot and need not replicate LCS permeability; rather, they must support vascular infiltration and interstitial fluid circulation, for which the 10^{-9} m^2 range measured in the present study is physiologically relevant.

2.4.2 Structural Origins of Topology-Dependent Permeability

The modest 11% permeability advantage of Gyroid over FKS is consistent with the structural data obtained from μCT (in Section 2.2.1). The wider mean wall spacing of FKS scaffolds (1.212 vs. 1.039 mm) and higher as-sintered porosity (74.00 vs. 68.49%) might initially be expected to favor permeability; however, the relationship between porosity, surface area, and permeability is not monotonic when topology changes simultaneously. This is precisely the scenario illustrated by Syahrom et al. [5] in their comparison of structures with identical porosity but different surface area: the higher-surface-area structure exhibited greater resistance to flow due to increased viscous dissipation at the fluid and solid interface, even though overall void fraction was unchanged.

In the present case, the marginally higher specific surface area of FKS (5.796 vs. 5.514 mm^{-1}) increases viscous drag relative to the Gyroid, partially offsetting the transport advantage of higher

porosity. Additionally, the larger wall spacing in FKS may be accompanied by greater pore tortuosity or more irregular channel interconnectivity relative to the smoother, more topologically uniform Gyroid network [13, 14]. Tortuosity is a well-established determinant of effective permeability in porous media: for a given porosity, structures with more tortuous flow paths exhibit systematically lower permeability because fluid parcels must travel longer effective distances to traverse a given scaffold length [1, 5]. The irregular pore channel geometry of FKS reflected in its greater coefficient of variation in wall thickness is consistent with a higher effective tortuosity that partially accounts for its lower permeability compared to Gyroid, despite nominally larger pores.

2.4.2 Flow-Rate Sensitivity and Mechanistic Interpretation

The statistically significant flow-rate dependence observed in FKS scaffolds ($p = 0.016$ and 0.001 for two measurement sets), absent in Gyroid scaffolds ($p = 0.341$), warrants careful interpretation. Since the Reynolds number remained below unity throughout, the flow is technically within the Darcian regime for both topologies and true Forchheimer-type inertial losses can be excluded as the primary explanation. The observed trend in apparent permeability increasing with increasing superficial velocity in FKS is more plausibly attributed to one of two mechanisms.

First, local inertial effects in geometrically complex pore junctions may become marginally relevant even at sub-unity Reynolds numbers in topologies with more irregular channel cross-sections. Vossenberg et al. [3] noted that the Navier–Stokes formulation captures the exact geometry of flow obstacles in a way that the Brinkman continuum model [3, 15]does not, and that differences between these approaches become more pronounced in architecturally complex systems. The FKS topology's greater structural heterogeneity evidenced by its higher wall thickness coefficient of variation may create local flow acceleration zones that contribute a small but detectable apparent velocity dependence to the bulk pressure–velocity relationship.

Second, progressive mobilization of trapped fluid pockets or reopening of marginally obstructed pore channels at higher flow rates could slightly increase the effective hydraulic cross-section available for flow. This mechanism is consistent with the observation that FKS scaffolds, with their wider and

more variable wall spacing, may contain a larger fraction of partially obstructed pore channels arising from sintering-induced defects or internal pore bridging. In contrast, Gyroid's smoother and more uniformly connected bicontinuous network is less susceptible to such partial obstruction, yielding more stable permeability values independent of flow rate.

These mechanistic interpretations are consistent with the general principle, established by Gascoin et al. [8] in the context of aerospace porous materials, that permeability characterisation using dynamic flow methods can be sensitive to both the measurement flow rate and the internal geometry of the porous medium. While Gascoin et al. developed their infrared spectroscopy approach specifically for real-time in-situ monitoring of permeability changes in metallic and ceramic matrix composite materials under extreme conditions, a context quite different from bone scaffold testing, their demonstration that even a 2% uncertainty in optical measurement translates to ~50% uncertainty in derived permeability emphasises the importance of rigorous calibration and methodology validation in any permeability study. The present study addresses this requirement through careful pressure transducer calibration (R^2 = 0.9695), the use of an elastomeric bypass-prevention sleeve, and triplicate measurements per condition.

2.4.3 Statistical Framework and Sample Size Considerations

The discrepancy between paired t-test (p = 0.055, non-significant) and ANOVA (p = 0.037, significant) outcomes for the between-architecture comparison illustrates the sensitivity of permeability study conclusions to the choice of statistical framework. The paired t-test, applied to initial measurements, treats within-scaffold variability as signal rather than noise when comparing topologies, thereby reducing statistical power for detecting modest between-group differences. ANOVA, by partitioning variance between and within groups, more appropriately accounts for scaffold-to-scaffold heterogeneity and reveals a statistically significant topology effect that the paired analysis obscures.

This distinction has practical implications for future scaffold permeability studies: where modest permeability differences (of order 10–20%) are expected between topologies, as is the case for

architecturally similar TPMS geometries, sample sizes of at least five specimens per group and ANOVA-based analysis frameworks are recommended to achieve adequate statistical power. The present study with n = 5 per topology is consistent with the sample sizes employed in comparable experimental permeability investigations [4, 5].

2.4.4 Implications for Bioreactor Design and Cell Culture

The permeability values measured in this study have direct implications for perfusion bioreactor design. Vossenberg et al. [**3**] established power-law relationships between Darcian permeability k_1 and average and maximum wall shear stress:

$$\tau_{\omega,avg} = 9.82 \times 10^{-12}. k^{-0.914} \quad (2.5)$$

$$\tau_{\omega,max} = 3.36 \times 10^{-10}. k^{-0.807} \quad (2.6)$$

The relationships derived by Zhao et al. for regular fibrous scaffolds represent order-of-magnitude estimates when applied to TPMS geometries due to their architectural differences from the fibrous systems for which the correlations were originally developed. Applying these relationships to the present permeability values, yields wall shear stress estimates that fall within the range associated with osteogenic stimulation at the flow rates used in the present study (1–5 mL/min). At lower permeabilities, such as those that might arise from cell-mediated reduction in effective pore volume during culture, shear stresses could increase substantially. The Gyroid's higher and more stable permeability therefore confers a degree of resilience against culture-induced increases in shear stress that may be biologically advantageous. These considerations reinforce that permeability is not merely a structural descriptor but a functional parameter with direct consequences for cell behaviour in dynamic culture systems.

2.4.5 FKS as a Viable Alternative to Gyroid

Although Gyroid scaffolds demonstrated statistically greater permeability, the absolute magnitude of the difference is modest relative to previously demonstrated mechanical advantages of the FKS architecture. This suggests that FKS may represent a viable alternative to Gyroid for load-bearing bone tissue engineering, where structural performance may take precedence over marginal differences in fluid transport behavior within a physiologically acceptable permeability range. The FKS permeability of $(1.13 \pm 0.06) \times 10^{-9}$ m^2 is not clinically limiting as it falls within the established range for bone tissue engineering scaffolds [1, 4] and supports adequate nutrient delivery at perfusion flow rates relevant to in vitro and in vivo environments. The key question, is whether the mechanical advantage of FKS is sufficiently large to justify its selection despite the modest permeability trade-off.

2.5 Conclusions

This study experimentally quantified the Darcian permeability of hydroxyapatite FKS and Gyroid scaffolds and evaluated topology-dependent fluid transport behavior under matched fabrication and testing conditions. The following principal conclusions are drawn:

(1) Both FKS and Gyroid architectures exhibited Darcian flow behavior ($Re < 1$) across all tested flow rates of 1–5 mL/min, confirming that the linear pressure–velocity relationship of Darcy's law is the appropriate transport model for these scaffold systems under the tested conditions.

(2) Gyroid scaffolds demonstrated statistically higher permeability ($1.27 \pm 0.20 \times 10^{-9}$ m^2) compared to FKS scaffolds ($1.13 \pm 0.06 \times 10^{-9}$ m^2), a difference of approximately 11% that became statistically significant ($p = 0.037–0.006$) when scaffold-to-scaffold variability was properly accounted for using ANOVA.

(3) FKS scaffolds exhibited mild but statistically significant flow-rate sensitivity ($p = 0.001–0.016$), plausibly attributable to the greater structural heterogeneity of the FKS topology following sintering. Gyroid scaffolds showed no significant flow-rate dependence ($p = 0.341$), consistent with the more uniform and well-connected bicontinuous channel network characteristic

of this topology. Measurement repeatability was confirmed for both topologies, validating the experimental protocol including the elastomeric sleeve bypass-prevention system and pressure transducer calibration.

(4) Both scaffold architectures fall within physiologically relevant permeability ranges for bone tissue engineering, approximately one order of magnitude below native vertebral cancellous bone permeability (~10^{-8} m^2). Achieving the physiological benchmark may require increased design porosity or alternative pore size parameters.

(5) The modest permeability advantage of Gyroid must be weighed against the comparative mechanical performance of FKS when selecting geometries for load-bearing applications. Within the framework established by Vossenberg et al. [3], both topologies produce permeability values sufficient to maintain cell-compatible shear stresses at the tested perfusion flow rates.

2.6 Bibliography

1. M. D. M. Innocentini, V. R. Salvini, A. Macedo, and V. C. Pandolfelli, "Permeability of porous gelcast scaffolds," Journal of Porous Materials, vol. 17, pp. 615–627, 2010.

2. E. A. Moreira, M. D. M. Innocentini, and J. R. Coury, "Permeability of ceramic foams to compressible and incompressible flow," Journal of the European Ceramic Society, vol. 24, pp. 3209–3218, 2004.

3. P. Vossenberg, G. A. Higuera, G. van Straten, C. A. van Blitterswijk, and A. J. B. van Boxtel, "Darcian permeability constant as indicator for shear stresses in regular scaffold systems for tissue engineering," Biomechanics and Modeling in Mechanobiology, vol. 8, pp. 499–507, 2009.

4. J. Santos et al., "On the permeability of TPMS scaffolds," Journal of the Mechanical Behavior of Biomedical Materials, vol. 110, 2020.

5. A. Syahrom, M. R. Abdul Kadir, J. Abdullah, and A. Öchsner, "Permeability studies of artificial and natural cancellous bone structures," Medical Engineering & Physics, vol. 35, pp. 792–799, 2013.

6. G. Baroud, J. Nemes, and E. J. Steffen, "Directional permeability of human vertebral cancel-lous bone," Journal of Biomechanics, vol. 37, pp. 189–196, 2004.

7. J. D. Gardinier, C. W. Townend, K.-P. Jen, Q. Wu, R. L. Duncan, and L. Wang, "In situ permeability measurement of the mammalian lacunar–canalicular system," Bone, vol. 46, pp. 1075–1081, 2010.

8. N. Gascoin, G. Fau, and P. Gillard, "Determination of Darcian permeability of porous material by infrared spectrometry," Journal of Porous Materials, vol. 19, pp. 317–331, 2012.

9. Y. Du et al., "Finite element analysis of mechanical behavior and permeability of porous

scaffolds," Materials Research Express, vol. 6, 2019.

10. L. Cardoso, S. P. Fritton, G. Gailani, M. Benalla, and S. C. Cowin, "Advances in assessment of bone porosity, permeability and interstitial fluid flow," Journal of Biomechanics, vol. 46, no. 2, pp. 253–265, 2013, doi: 10.1016/j.jbiomech.2012.10.025.

11. V. Karageorgiou and D. Kaplan, "Porosity of 3D biomaterial scaffolds and osteogenesis," Biomaterials, vol. 26, no. 27, pp. 5474–5491, 2005, doi: 10.1016/j.biomaterials.2005.02.002.

12. S. Melchels et al., "Additive manufacturing of TPMS scaffolds," Biomaterials, vol. 31, pp. 6909–6916, 2010.

13. Y. Lu, W. Zhao, Z. Cui, H. Zhu, and C. Wu, "The anisotropic elastic behavior of the widely-used triply-periodic minimal surface based scaffolds," Journal of the Mechanical Behavior of Biomedical Materials, vol. 99, pp. 227–239, 2019, doi: 10.1016/j.jmbbm.2019.07.018.

14. V. Baumer, N. Isaacson, S. Kanakamedala, D. McGee, I. Kaze, and D. Prawel, "Comparing ceramic Fischer-Koch-S and gyroid TPMS scaffolds for potential in bone tissue engineer-ing," Frontiers in Bioengineering and Biotechnology, vol. 12, art. 1410837, 2024, doi: 10.3389/fbioe.2024.1410837.

15. H. C. Brinkman, "A calculation of the viscous force exerted by a flowing fluid on a dense swarm of particles," Applied Scientific Research, vol. 1, no. 1, pp. 27–34, 1949, doi: 10.1007/BF02120313.

Chapter 3

Evaluation of Adhesive and Attachment Methods for Strain Gauge Application on Porous Scaffolds

3.1 Introduction

Accurate measurement of strain in porous scaffold structures is a prerequisite for reliable mechanobiological interpretation, yet it presents unique challenges that distinguish these substrates from conventional smooth, homogeneous test specimens. The geometric irregularity, inherent surface porosity, and material heterogeneity of additively manufactured scaffolds each introduce potential sources of measurement error that must be systematically addressed before strain data can be used with confidence. Central to this challenge is the role of the adhesive interlayer, which mediates all mechanical communication between the substrate and the sensing grid of an electrical resistance strain gauge.

Electrical resistance strain gauges do not directly measure substrate strain; rather, they record the strain transmitted through the adhesive layer bonding them to the surface. Classical strain-transfer theory demonstrates that shear lag develops across the adhesive thickness as a result of modulus mismatch between the substrate and adhesive, creating strain gradients that attenuate the signal reaching the gauge [1]. Even for nominally thin adhesive layers, this attenuation can be significant, and it is governed primarily by the shear modulus and thickness of the interlayer. The adhesive therefore functions as a mechanical filter: one that ideally transmits strain with high fidelity, but in practice introduces systematic error when its compliance or thickness is not carefully controlled.

Experimental evidence corroborates this theoretical framework. Komurlu et al. reported errors exceeding 100% in measured elastic modulus as a function of adhesive stiffness and thickness, with strain loss across compliant interlayers reaching up to 51% [2]. These findings underscore

that adhesive selection is far from trivial as it is a factor capable of fundamentally distorting the measured mechanical response. This problem is compounded when the substrate departs from the idealized, polished metallic surface that characterizes most strain gauge validation studies.

Additively manufactured scaffolds produced by melt extrusion and viscous ceramic paste extrusion present precisely such a departure. The extrusion process inherently yields micro-voids, filament ridges, and reduced surface continuity, all of which interfere with adhesive bonding in ways that do not occur on machined metallic or dense polymer specimens. When an adhesive is applied to such a surface, it may infiltrate the surface porosity rather than forming a uniform thin film, thereby increasing the effective interlayer thickness and altering local compliance [3]. The resulting variability in bonding efficacy means that the mechanical filtering effect of the adhesive is not only present but spatially non-uniform.

This interaction between adhesive behavior and substrate microstructure establishes a direct link between attachment protocol and the quality of strain data used for mechanobiological modeling. It should be noted that the present study employs a constitutive mapping approach unique to this work: surface principal strains are measured experimentally on PLA Gyroid scaffold surrogates and subsequently transformed into ceramic-equivalent strain fields using the ratio of elastic compliances between the PLA and hydroxyapatite scaffold architectures. Because subsequent scaffold performance is evaluated by transforming surface strain measurements into ceramic-equivalent strain fields and interpreting them against established mechanoregulation thresholds [4, 5], any systematic attenuation or variability introduced at the adhesive interface propagates directly into the biological conclusions.

The objective of this chapter is to confirm the literature with our test materials, by experimentally comparing two adhesive systems: a high-modulus cyanoacrylate and a low-modulus elastomeric adhesive for strain gauge bonding to porous polylactic acid (PLA) gyroid scaffolds, and to quantify their influence on the magnitude and repeatability of measured principal strain. The adhesive system identified as superior in this evaluation was subsequently adopted as the standard attachment protocol for all strain gauge installations on hydroxyapatite ceramic scaffold constructs reported

in Chapters 3 and 4, on the basis that both substrate types share comparable surface morphology characteristics arising from the robocasting fabrication process.

3.2 Materials and Methods

3.2.1 Scaffold Preparation

Gyroid 30 mm cubic scaffolds (70% nominal porosity) were fabricated using melt extrusion fabrication (PLA). Surface roughness and micro-porosity inherent to the extrusion process required sanding prior to gauge bonding.

3.2.2 Adhesive Systems

Two adhesive systems were investigated: M-Bond 200 (cyanoacrylate-based, high-modulus adhesive) and Biomed Elastic 50A (low-modulus elastomeric adhesive). Cyanoacrylate adhesives are widely used in strain gauge mounting applications due to their high stiffness and thin bonding layers, which promote efficient strain transfer [3]. In contrast, elastomeric adhesives introduce compliance at the interface and are expected to increase shear-lag effects [2].

3.2.3 Gauge Installation Protocol

For M-Bond 200, the adhesive was employed both as a surface sealant and bonding agent. A thin layer was first applied to the designated bonding region to fill micro-porosities inherent to the PLA print structure. A minimal quantity of adhesive was then applied to the backing of the strain gauge. The gauge was transferred from a glass slab onto the prepared scaffold region, ensuring alignment with the principal loading axis. Gentle pressure was applied to promote uniform adhesive distribution. Assemblies were cured undisturbed at ambient laboratory temperature (22–24 $^{\circ}$C) for a minimum of 12 hours to ensure complete polymerization. The elastomeric adhesive group followed identical placement procedures; however, visual inspection indicated increased interlayer

thickness due to reduced capillary infiltration into surface porosity. Gauge preparation and bonding procedures followed the general protocols described by Cordey and Gautier [9].

3.2.4 Mechanical Testing and Strain Analysis

Specimens were subjected to controlled compressive loading using a uniaxial testing machine across all experimental groups. Load was applied quasi-statically at a rate of 0.5 mm/min to a maximum compressive force of 1000 N or till failure of the PLA scaffold material. Load and displacement data were recorded simultaneously with strain gauge output.

Strain measurement was performed using rectangular (0°/45°/90°) three-element rosette gauges (Micro-Measurements, model CEA-06-062UR-350) bonded to the scaffold surface. This rosette configuration was selected because compressive loading of a gyroid scaffold does not in general produce a uniaxial surface strain state; the complex geometry generates biaxial strain fields in which the directions of principal strain are not known [7]. A rectangular rosette permits recovery of the full in-plane strain tensor from three independent gauge readings, enabling determination of both the principal strain magnitudes and their orientations without prior knowledge of the loading geometry [6, 9].

Each rosette element was connected in a quarter-bridge Wheatstone circuit configuration using a three-wire connection scheme. The three-wire arrangement was employed to minimise errors due to leadwire resistance variation, which can be significant when long lead wires are used or when ambient temperature fluctuates during testing [6]. In a three-wire quarter-bridge, the resistance of the leadwire connecting the gauge to the completion resistors is shared between the two arms of the bridge, so that thermal changes in leadwire resistance produce equal and opposing effects that largely cancel one another, substantially reducing measurement error relative to a two-wire configuration.

Raw bridge output voltages from the three rosette elements were acquired using a National Instruments data acquisition system at a sampling rate of 1000 Hz. The gauge excitation voltage was set to 2.0 V to limit self-heating effects in the bonded gauge, consistent with recommendations

for polymeric substrates with low thermal conductivity [7]. Prior to loading, all channels were balanced and zeroed to remove any residual offset due to pre-existing thermal strains or slight gauge misalignment.

Measured bridge voltages were converted to individual element strains using the standard linear gauge equation:

$$\varepsilon = (4 \times \Delta V/V^e) / (GF \times (1 + 2 \times \Delta V/V^e)) \quad (3.1)$$

where ε is the measured strain, $\Delta V/V_e$ is the bridge output ratio, and GF is the gauge factor ($GF = 2.085 \pm 0.5\%$).

Principal strains were subsequently calculated from the three rosette element strains (ε_1, ε_2, ε_3 at 0°, 45°, and 90°) using standard rectangular rosette transformation equations [9]:

$$\varepsilon\_max\ ,\ \varepsilon\_min = (\varepsilon_1 + \varepsilon_3)/2 \pm (1/\sqrt{2}) \times \sqrt{[(\varepsilon_1 - \varepsilon_2)^2 + (\varepsilon_2 - \varepsilon_3)^2]} \quad (3.2)$$

The angle θ of the maximum principal strain axis relative to the 0° gauge element: $\tan(2\theta) = (2\varepsilon_2 - \varepsilon_1 - \varepsilon_3) / (\varepsilon_1 - \varepsilon_3)$ (3.3)

The maximum principal strain magnitude (ε_max) was selected as the primary comparison metric between adhesive groups, as it represents the most mechanobiologically relevant quantity for interpreting tissue differentiation stimuli [4, 5, 8]. This choice is consistent with the approach used in experimental bone strain studies, in which principal surface strains are used to validate computational loading models and establish dose-response relationships between mechanical stimulation and tissue adaptation [8, 10].

All signal processing and principal strain calculations were performed in MATLAB (MathWorks, R2023b). For each specimen, the mean principal strain across the plateau region of the loading curve (10–40 N) was computed to provide a single representative value per gauge site. This approach minimised the influence of any transient effects at the onset of loading while remaining within the linear elastic deformation regime of the scaffold material.

3.2.5 Statistical Analysis

Experimental groups were defined according to adhesive type and replicate condition. One-way ANOVA was performed to assess differences between groups. Statistical significance was defined at $\alpha = 0.05$.

3.3 Results

3.3.1 Principal Strain Magnitudes

M-Bond 200 specimens produced principal strain magnitudes in the range of approximately 0.026–0.031. Elastic 50A specimens exhibited principal strains up to approximately 0.0629, with substantially greater variability.

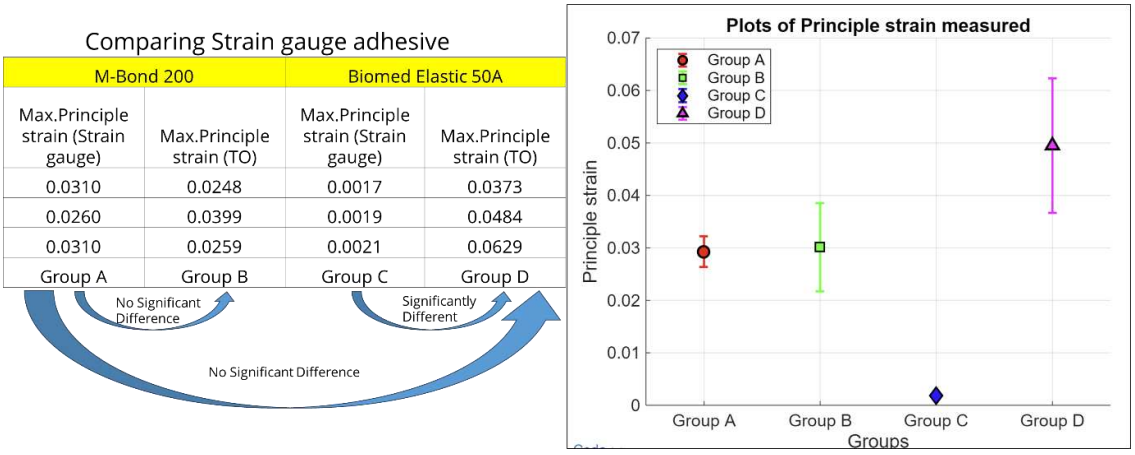

Figure 3.1: Comparing Strain measured by the bench top UTM (Tinius Olsen) to the strain measured by strain gauges attached by the different gauge adhesive

3.3.2 Statistical Comparisons

Statistical comparisons revealed a significant difference in replicate consistency between adhesive groups. The M-Bond replicate comparison yielded $p = 0.874$ (not significant), indicating high reproducibility. In contrast, the Elastic 50A replicate comparison yielded $p = 0.003$ (significant), confirming that the elastomeric adhesive introduced substantial inter-specimen variability.

These results indicate that adhesive modulus significantly influences both strain magnitude and measurement repeatability.

3.4 Discussion

3.4.1 Adhesive Modulus and Shear-Lag Effects

The results confirm the theoretical prediction that compliant adhesives reduce strain-transfer fidelity. Strain-transfer efficiency is governed by adhesive shear stiffness and thickness, as predicted by classical shear-lag models [1]. A compliant adhesive increases interfacial shear deformation, attenuating the strain transmitted to the gauge and introducing spatial non-uniformity beneath the sensing grid. The substantially elevated and variable strain magnitudes observed in the Elastic 50A group are consistent with this mechanism and are further supported by the findings of Komurlu et al., who demonstrated that compliant adhesives can produce substantial modulus measurement error [2].

3.4.2 Influence of Porous Substrate

The porous nature of the melt extrusion fabricated scaffolds amplified the differences between adhesive systems. On these substrates, adhesive infiltration into surface voids alters local interlayer thickness and compliance in a spatially non-uniform manner. The elastomeric adhesive likely formed thicker, irregular interlayers within surface voids, amplifying strain redistribution effects and contributing to the high inter-specimen variability observed statistically. Conversely, the low variability of M-Bond 200 is consistent with the behavior of thin, high-modulus adhesives described in the strain gauge literature [3].

3.4.3 Implications for Mechanobiological Interpretation

Because scaffold strains in this study are transformed into ceramic-equivalent strain fields and interpreted against osteogenic or fibrotic thresholds [4, 5], systematic underestimation or inflated

variability at the adhesive interface could result in misclassification of the mechanical environment. Accurate and repeatable strain transfer is therefore not only metrologically desirable but scientifically essential for the translational integrity of subsequent modeling work.

3.5 Conclusions

This study demonstrated that adhesive selection significantly affects both the magnitude and repeatability of strain measurements on porous scaffolds. The cyanoacrylate adhesive M-Bond 200 provided consistent strain transfer, exhibited low inter-specimen variability, and minimized shear-lag effects is behavior attributable to its high modulus and ability to form a thin, uniform bonding layer even on irregular met extruded surfaces. The elastomeric adhesive Elastic 50A produced elevated and highly variable strain readings, consistent with the shear-lag effects predicted by classical strain transfer theory [1, 2].

Based on these findings, thin, high-modulus cyanoacrylate adhesives are recommended for strain gauge application on porous scaffold substrates. These results establish a standardized bonding protocol for subsequent scaffold mechanobiology studies, and underscore that adhesive selection must be treated as a primary methodological consideration whenever surface strain data are to be used for mechanobiological modeling.

3.6 Bibliography

1. H. Stehlin, "Strain Distribution In and Around Strain Gauges," Hottinger Baldwin Messtechnik, Technical Report, 1972.

2. E. Komurlu, F. Cihangir, A. Kesimal, and S. Demir, "Effect of Adhesive Type on the Measurement of Modulus of Elasticity Using Electrical Resistance Strain Gauges," Arabian Journal for Science and Engineering, vol. 41, no. 2, pp. 433–441, 2016.

3. Micro-Measurements (VPG), "Strain Gauge Installations with M-Bond 200 Adhesive," Instruction Bulletin B-127, Vishay Precision Group, Malvern, PA.

4. L. E. Lanyon, "Functional Strain in Bone Tissue as an Objective, and Controlling Stimulus for Adaptive Bone Remodelling," Journal of Biomechanics, vol. 20, no. 11–12, pp. 1083–1093, 1987.

5. L. E. Lanyon, "Functional Strain as a Determinant for Bone Remodeling," Calcified Tissue International, vol. 36, pp. S56–S61, 1984.

6. Micro-Measurements (VPG), "The Three-Wire Quarter-Bridge Circuit," Tech Note TT-612, Vishay Precision Group, Malvern, PA.

7. Micro-Measurements (VPG), "Stacked Rosette Strain Gage G1350A – Data Sheet," Vishay Precision Group, Malvern, PA.

8. R. Steck, P. Niederer, and M. L. Knothe Tate, "A Finite Element Analysis for the Prediction of Load-Induced Fluid Flow and Mechanochemical Transduction in Bone," Journal of Theoretical Biology, vol. 220, no. 2, pp. 249–259, 2003.

9. J. Cordey and E. Gautier, "Strain Gauges Used in the Mechanical Testing of Bones, Part II: 'In Vitro' and 'In Vivo' Technique," Injury, vol. 30, Suppl. 1, pp. SA14–SA20, 1999.

10. B. B. Mikic´ and D. R. Carter, "Bone Remodeling Theory Based on Intrinsic Microdamage in the Context of the Utah Paradigm," Journal of Orthopaedic Research, vol. 13, no. 1, pp. 74–81, 1995.

11. C. B. Frank, N. G. Shrive, D. A. Hart, and H. A. Bray, "A Versatile Shear and Compression Apparatus for Mechanical Stimulation of Tissue Culture Explants," Medical Engineering & Physics, vol. 22, no. 8, pp. 575–579, 2000.

Chapter 4

Study of Effects of 3D Printed Polycaprolactone Sleeve on Transverse Strain in Critical-Sized 3D Printed Gyroid Scaffold

4.1 Introduction

Calcium phosphate ceramics, particularly apatite-based compositions, remain among the most clinically relevant materials for bone tissue engineering owing to their chemical similarity to the mineral phase of native bone. This compositional mimicry promotes osteoconduction, cellular attachment, and mineral deposition in ways that synthetic polymers and metals cannot replicate. However, apatite scaffolds are inherently brittle, with limited fracture toughness, a mechanical limitation that has historically restricted their use in human-scale load-bearing long-bone reconstructions where failure would have serious clinical consequences.

Advances in scaffold architecture, particularly the adoption of TPMS topologies, have improved the structural efficiency of ceramic scaffolds without requiring increases in material density. Among available TPMS geometries, the Gyroid provides continuous, fully interconnected pore networks, reduces stress concentration sites relative to stochastic foam architectures, and improves load distribution through its periodic curvature. These architectural advantages enhance mechanical performance at a given porosity but do not eliminate the intrinsic brittleness of the ceramic constituent.

The mechanobiological significance of this susceptibility is grounded in established fracture healing theory. Mechanoregulatory frameworks developed by Carter and subsequently formalized by Claes and Heigele demonstrate that local strain magnitude governs tissue differentiation at a regenerating defect site. Moderate compressive strains promote endochondral ossification and direct

bone formation, while excessive tensile or shear strain redirects tissue fate toward endochondral ossification resulting in fibrous, poorly formed bone tissue which impairs union.

Conventional strategies for improving ceramic scaffold toughness involve polymer composite fabrication, surface infiltration, or coating approaches. While these methods can enhance fracture toughness, they introduce significant trade-offs: polymer infiltration reduces pore interconnectivity, alters degradation kinetics, masks the osteoconductive ceramic surface and reduces total bone volume, as polymers must degrade before bone tissue can replace them.

The present study proposes a external reinforcement strategy in which the protective polymeric component is positioned externally rather than integrated within the scaffold matrix. The central hypothesis is that an externalized polycaprolactone (PCL) sleeve can reduce transverse strain within a brittle, highly porous Gyroid apatite scaffold while preserving the physiologic axial compressive strain required to support osteogenesis.

To evaluate this hypothesis, an investigation was conducted using an established ovine metatarsal critical defect model. Highly porous PLA Gyroid scaffolds with and without a PCL sleeve were subjected to cyclic, human-scale compressive loading of a critical-sized defect supported by a steel fixation please which was installed in accordance with typical surgical norms. Multiaxial surface strain was quantified using rosette strain gauges and mapped to ceramic-equivalent values through a constitutive transformation framework.

4.2 Materials and Methods

4.2.1 Sleeve Design and Fabrication

The endoprosthetic sleeve was fabricated from Facilan^{TM} PCL 100 Filament (80 kDa, 3D4Makers, Netherlands), a medical grade polycaprolactone selected for its biocompatibility, biodegradability, and thermal processability. The sleeve was designed to mechanically encapsulate the Gyroid scaffold, providing a conformal interface replicating the outer geometry of the excised ovine metatarsal segment. Scaffold and sleeve dimensions were derived from computed tomography data

of a representative adult ovine metatarsus. Geometry was developed in SolidWorks (Dassault Systèmes), with both external contours and internal cavities parametrically modeled to achieve a slip-fit tolerance with the scaffold. Other aspects of the sleeve geometry such as wall thickness, fenestration and coupling to the fixation plate were developed in other research in our laboratory. Finalized geometries were exported as STL files and processed in PrusaSlicer. Fabrication was performed on a Prusa melt extrusion printer with nozzle temperature calibrated to 125–135 °C, bed temperature 35°C, print speed 10~mm/s, and 100% fan cooling supplemented by an external fan directed at the printed layer to ensure rapid solidification and dimensional stability of the low melting point PCL filament.

4.2.2 Scaffold Fabrication

Gyroid scaffold models were generated using a previously described computational method [1]. The Gyroid surface was defined by the trigonometric approximation:

$$\sin(y)\cos(x) + \sin(z)\cos(y) + \sin(x)\cos(z) = 0 \quad (4.1)$$

Scaffolds were designed as 30 mm cubic constructs with nominal porosity of approximately 70% and pore size of approximately 1 mm. A single road width of 0.413 mm defined wall thickness. Each scaffold was divided into interlocking distal and proximal regions connected through crenulation style junctions to ensure mechanical continuity.

Scaffolds were fabricated using melt extrusion on Bambu 3D printers utilizing PLA filament. PLA was selected as the surrogate fabrication material for two reasons: first, it permitted high-resolution printing of Gyroid TPMS geometry with dimensional accuracy sufficient to replicate the wall thickness and pore size of the ceramic constructs used in subsequent chapters; and second, its melt extruded surface morphology characterized by filament ridges and road boundary features comparable to those of robocast hydroxyapatite scaffolds provided a representative substrate for evaluating strain gauge adhesive performance under surface conditions relevant to the ceramic system. Strain values measured on PLA scaffolds were subsequently transformed to ceramic-equivalent values through the constitutive mapping

described in Section 4.2.6. Following printing, the anterior face of each scaffold was manually sanded with fine grit sandpaper and surface debris removed with isopropyl alcohol to ensure consistent gauge seating across specimens.

Figure 4.1: PCL sleeve

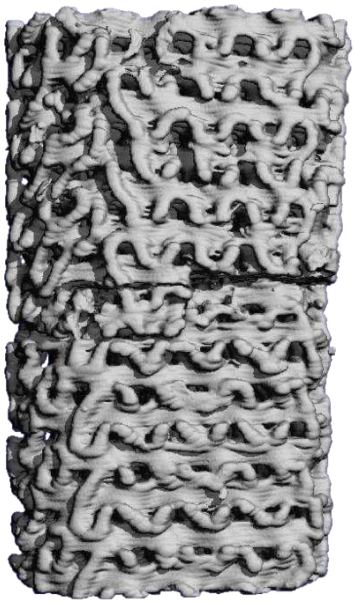

Figure 4.2: Representative images and micro-CT scans of 3D-printed and sintered scaffolds

4.2.3 Strain Gauge Attachment

Multiaxial surface strain was measured using C4A-39P-G1350A-120 rosette strain gauges (Micro-Measurements) configured in a $0^{\circ} / \pm 45^{\circ}$ orientation. Gauge placement positions were marked on the sanded scaffold face guided by prior marked of sections. MBond 200 adhesive was applied both as a surface sealant to fill microporosities and as the primary bonding agent [7]. All assemblies were cured undisturbed at ambient room temperature (22–24 $^{\circ}$C) for a minimum of 12 hours.

4.2.4 Bone Preparation and Defect Creation

Necropsied ovine hindlimbs were obtained and maintained in chilled phosphate-buffered saline. All soft tissues were dissected from the bone surface. Metatarsal bones were isolated from surrounding tarsal and phalangeal structures.

Each metatarsal was aligned and a 3.5 mm Locking Compression Plate (LCP) (Movora, Florida) was installed in accordance with common surgical practice. The LCP was positioned on the lateral cortex to serve as a positional reference for demarcating the osteotomy boundaries, ensuring that the 30mm segmental defect would be centered within the plate span. The central segment along the mid-diaphysis was demarcated, flanked by three cortical screw holes on both proximal and distal ends. Pilot holes were created using manufacturer-supplied drill guides. Self-tapping cortical screws were inserted to affix the LCP. The plate was then temporarily detached, transverse osteotomies were performed at the premarked boundaries using a bone band saw [8], and the excised segment was discarded. The LCP was reassembled and all screws reinserted to restore stable fixation.

Two experimental groups were evaluated: a scaffold alone bridging the 30 mm defect, and a sleeved group in which the PCL sleeve was positioned concentrically around the scaffold before fixation. This configuration enabled direct comparison of strain response between groups under identical boundary and loading conditions.

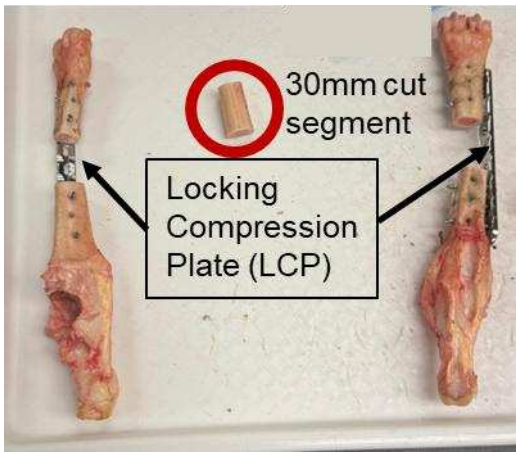

Figure 4.3: 30 mm central segment along the mid-diaphysis cut and LCP reassembled

4.2.5 Mechanical Loading Protocol

Cyclic compressive loading was performed using a modified Incudyn compression testing apparatus, a biaxial tissue-loading device originally developed at the Massachusetts Institute of Technology capable of prescribing precise axial displacements and sinusoidal waveforms via computer interface [12] configured for uniaxial sinusoidal compressive loading of scaffold-bone assemblies. Scaffold–bone assemblies were mounted between precision-machined stainless-steel grips to maintain axial alignment and prevent rotational slip.

The load range of 0–150 N was selected based on physiologic loading estimates for the ovine metatarsus during ambulation. Kinetic gait analyses in sheep report mean peak vertical forces of approximately 38.5% of body weight in the hindlimbs during the stance phase [10]. For a 60 kg sheep, this corresponds to a peak hindlimb force of approximately:

$$0.4 \times 60\,\text{kg} \times 9.81\,\text{m/s}^2 \approx 235\,\text{N} \quad (4.2)$$

The 150 N cyclic regime represents a conservative sub-peak value that achieves mechano-biologically relevant strain magnitudes while ensuring the scaffold, sleeve and LCP remain within their respective elastic regimes. Five independent bone–scaffold assemblies were tested in each group (n = 5), with three sinusoidal loading cycles applied per test, repeated three times per specimen.

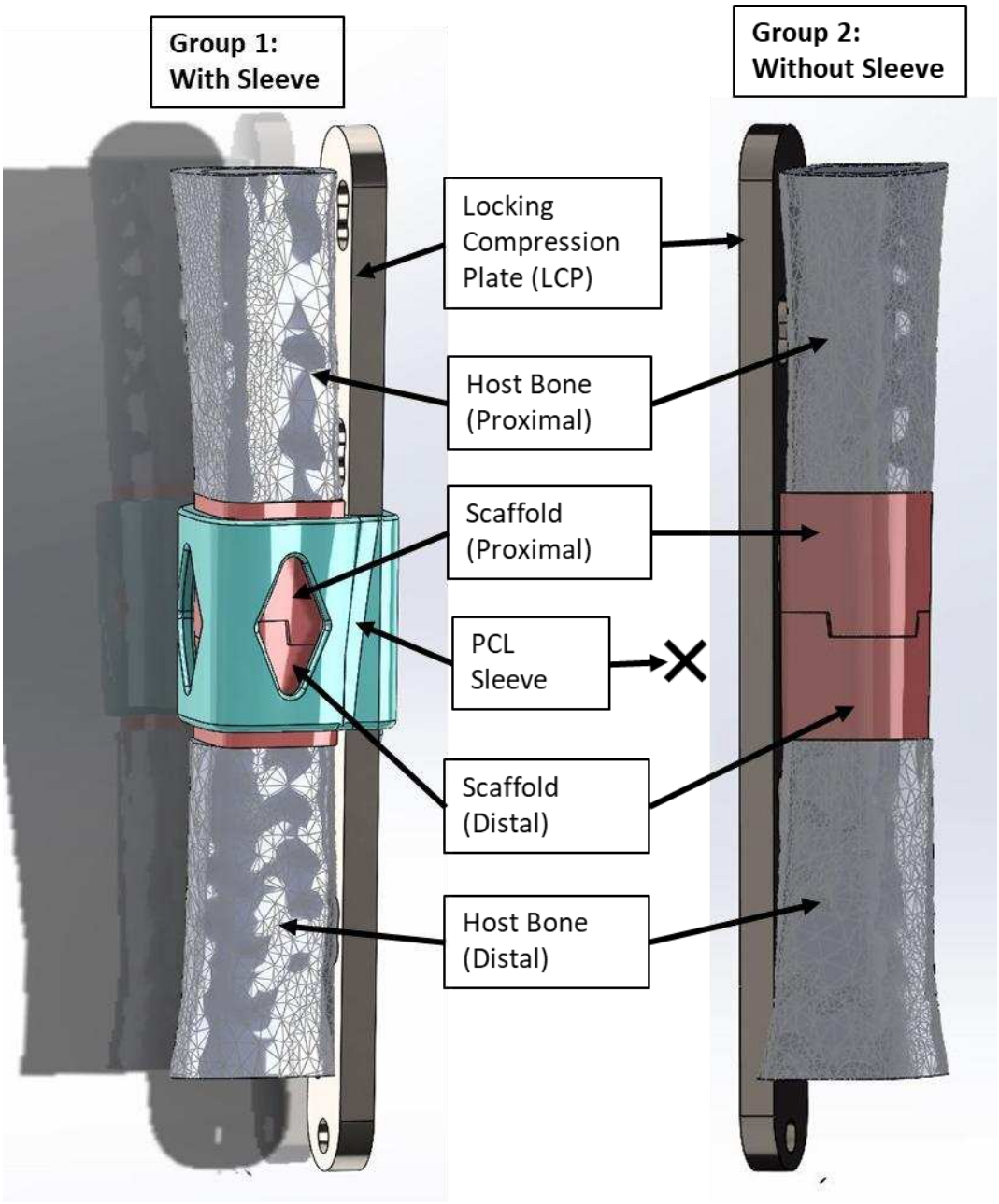

Figure 4.4: experimental groups that were evaluated

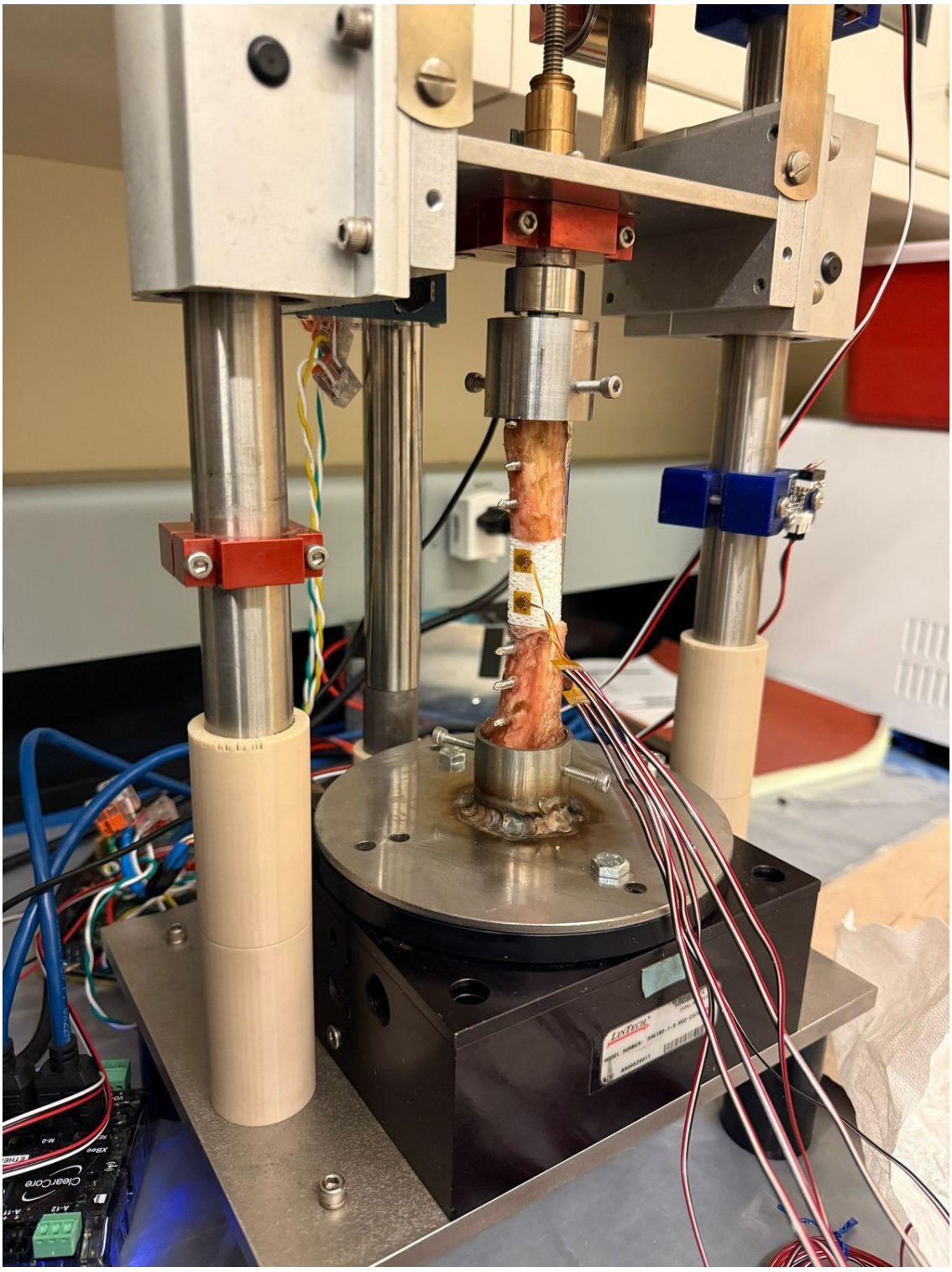

Figure 4.5: Incudyne compression testing machine with bone scaffold assembly

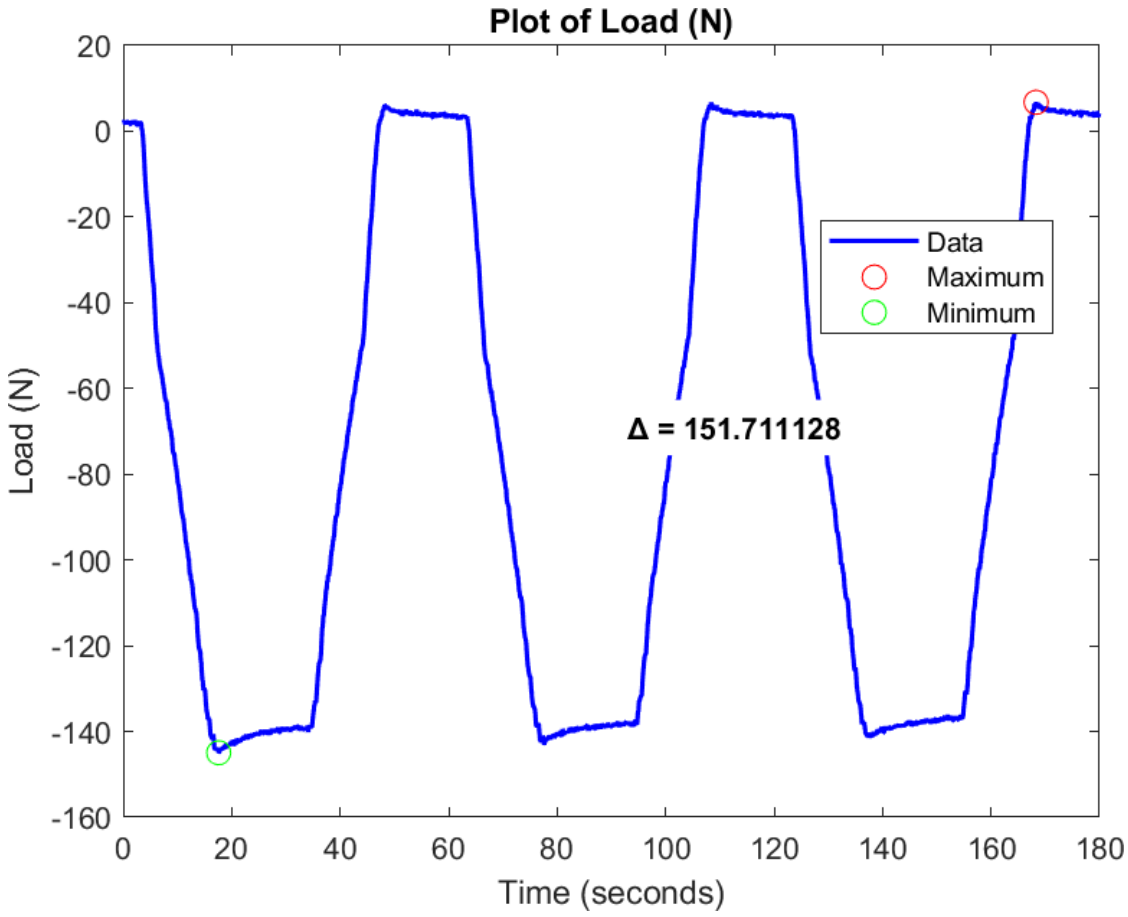

Figure 4.6: Loading cycle on the Incudyne

4.2.6 Data Collection and Strain Transformation

Voltage signals from the rosette gauges were recorded in real time using an NI-9219 DAQ module interfaced with MATLAB and converted to strain using manufacturer calibration constants. Each cyclic dataset was baseline corrected to eliminate thermal drift. To ensure a conservative and representative comparison between groups, the single cycle exhibiting the maximum deviation in peak strain among the three repeated tests was selected for reporting.

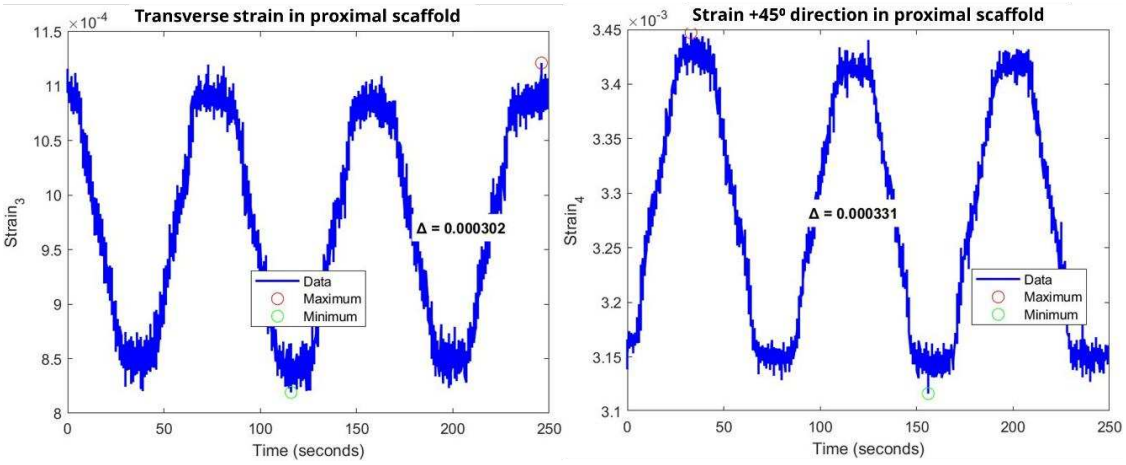

Figure 4.7: Raw strain data after zero correction

Raw strain data were resolved into axial (ε_x), transverse (ε_y), and in-plane shear (γ_{xy}) components using standard strain-transformation relations. Principal strains and orientations were determined from Mohr's circle analysis[13].

Bulk material properties were characterized independently. Compression tests on solid PLA calibration cubes yielded $E_1 \approx 2.2$ GPa and $\nu_1 \approx 0.35$. Similar tests on ovine bone mineral (OBM) ceramic cubes — the same deproteinized bovine-derived hydroxyapatite material from which the ceramic scaffolds in Chapters3 and 4. yielded $E_2 \approx 6.0$ GPa and $\nu_2 \approx 0.42$.

Assuming linear-elastic isotropic behavior for both materials within the applied strain range (< 2% nominal deformation), PLA strain vectors were transformed to ceramic-equivalent strain values according to:

$$\boldsymbol{\varepsilon}_2 = \mathbf{S}_2\,(\mathbf{C}_1\boldsymbol{\varepsilon}_1) \quad (4.3)$$

where $\boldsymbol{\varepsilon}_1$ is the experimentally measured PLA strain vector, $\mathbf{C}_1$ is the PLA stiffness matrix, $\mathbf{S}_2$ is the OBM compliance matrix, and $\boldsymbol{\varepsilon}_2$ is the resulting ceramic-equivalent strain vector.

The constitutive mapping expressed in Equation 4.3 is justified on the following grounds. Both PLA and OBM ceramic exhibit linearly elastic behavior within the applied strain range of less than 2% nominal deformation, meaning that the stress-strain relationship in each material is fully characterized by a fixed, load-independent stiffness matrix with no viscoelastic, plastic, or damage-dependent contributions at these strain levels[13]. Under this condition, the stress state within the scaffold walls produced by a given external load is uniquely determined by the applied boundary conditions and the material stiffness, and the corresponding strain state is uniquely recovered by applying the material compliance. Because the PLA surrogate scaffolds and the OBM ceramic scaffolds share identical Gyroid topology, nominal porosity, and unit cell geometry, the distribution and orientation of the internal strain field i.e., regions experience tension, compression, or shear, and in what proportions are governed by scaffold architecture rather than material constitution. The constitutive mapping therefore scales the experimentally measured PLA strain magnitudes by the ratio of elastic compliances between the two materials while preserving the strain field pattern, yielding ceramic-equivalent strain values that reflect what the OBM scaffold walls would experience

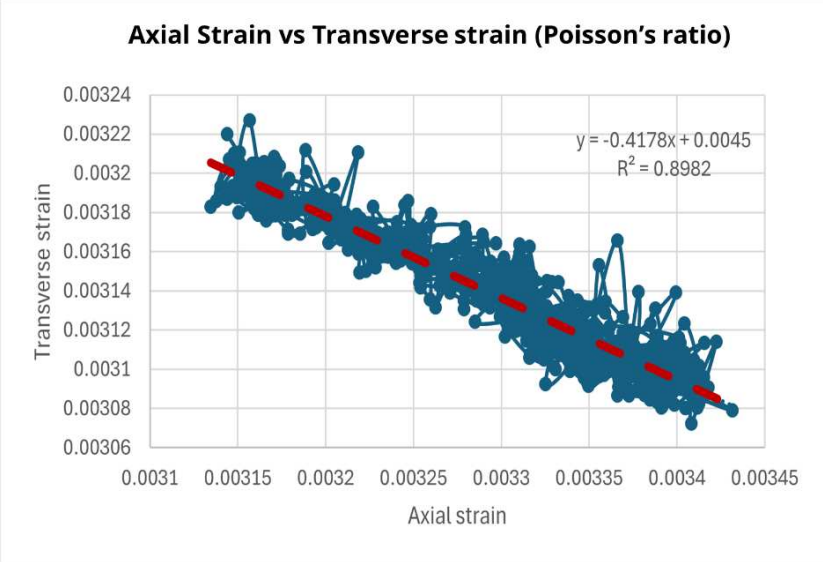

Figure 4.8: Poisson's ratio plots from Compression tests on gyroid OBM calibration cubes

under the same external loading and boundary conditions. This approach is analogous to the use of photoelastic or polymer surrogate models in experimental stress analysis, where a geometrically identical but mechanically distinct surrogate is used to infer stress and strain distributions in a target material through a known constitutive relationship[14].

4.2.7 Statistical Analysis

Peak principal strain values from sleeved and unsleeved constructs were compared using an independent-samples *t*-test, with statistical significance set at $p < 0.05$. Cycle-to-cycle repeatability was assessed by computing the coefficient of variation across repeated test sequences. All analyses were performed in MATLAB.

4.3 Results

4.3.1 Loading Response and Repeatability

Scaffold–bone assemblies subjected to sinusoidal cyclic loading between 0 and 150 N exhibited stable and repeatable load–strain responses. Minor viscoelastic settling was observed during the first cycle, after which strain amplitudes stabilized. Cycle-to-cycle variability in recorded strain did not exceed $\pm 5\ \mu\varepsilon$, and repeatability error between replicate specimens remained within 6%. Baseline noise following band pass signal filtering was below $2\ \mu\varepsilon$.

4.3.2 Strain Decomposition and Principal Directions

The dominant deformation mode was axial compression in both experimental groups, with measurable transverse expansion and negligible in-plane shear. Principal strain orientations determined from Mohr's circle analysis remained nearly collinear with the loading axis in both groups, confirming the geometric symmetry of the Gyroid lattice under axial compression and validating the assumption of effective macroscopic isotropy used in the constitutive transformation.

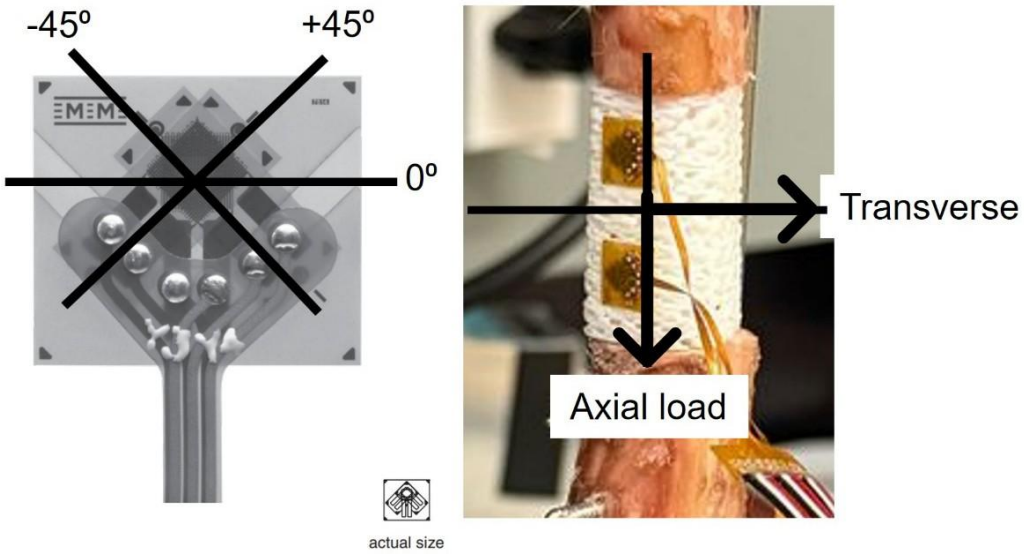

Figure 4.9: (A) Rosette strain gauge element orientations (0˚/ 45˚) shown at actual size. (B) Gauge mounted on the anterior face of a scaffold–bone construct with coordinate axes indicating the axial loading direction and transverse direction. The 0˚ gauge element was aligned with the transverse axis.

4.3.3 Ceramic-Equivalent Strain Magnitudes

Following constitutive transformation, OBM-equivalent principal strain magnitudes ranged between 200 and 300 $\mu\varepsilon$ across all specimens. These values are consistent with reported physiologic strain levels in healthy cortical bone during ambulation (100–400 $\mu\varepsilon$ [2, 4]) and fall within the mechanobiological window associated with bone maintenance and adaptive remodeling.

4.3.4 Effect of the PCL Sleeve on Strain Distribution

Assemblies incorporating the sleeve exhibited a statistically significant reduction in transverse strain while axial compressive strain magnitudes remained comparable between groups. This indicates that the sleeve selectively attenuated the transverse deformation components arising from the combination of Poisson-effect lateral strain through the scaffold pore network without attenuating the axial compressive stimulus. Mean transverse strain in the sleeved group decreased to approximately 0.3%, lower than values recorded in the unsleeved group, and well below the 5% threshold associated with the strain domain that mechanoregulation models associate with intramembranous ossification.

The reduction in transverse expansion indicates that the sleeve redistributed compressive load more uniformly across the scaffold perimeter, suppressing the localized bending of Gyroid strut walls that drives transverse deformation under axial loading. No evidence of gauge delamination or signal drift was observed throughout testing.

Figure 4.10: Statistically significant reduction in transverse strain due to the sleeve on a ceramic scaffold

4.4 Discussion

The principal finding of this study is that an external PCL sleeve can selectively reduce transverse strain within a highly porous Gyroid apatite scaffold while preserving axial compressive strain within the osteogenic range. This result supports the central hypothesis and demonstrates that mechanical modulation of the scaffold strain environment can be achieved through an external constraint without altering scaffold composition, porosity, or surface bioactivity. The following discussion addresses the mechanistic basis of this finding, the assumptions underlying the constitutive transformation framework, the physiologic relevance of the loading protocol, and the limitations that should inform interpretation of these results.

The selective reduction of transverse strain by the sleeve is consistent with its role as a conformal external constraint that intercepts the lateral expansion generated by axial Poisson effects and

localized strut bending. Under axial compression, the Gyroid lattice transmits load through its continuous curved walls, which develop both compressive and bending stresses depending on their local orientation relative to the loading axis. The PCL sleeve, positioned concentrically around the scaffold perimeter, creates a stiffness mismatch at the outer boundary that redistributes these bending dominated deformations around the scaffold rather than through it. Because PCL is substantially more compliant than the ceramic it would replace in a composite strategy, this redistribution occurs without introducing the axial stiffening that would characterize a fully infiltrated composite and without generating the stress shielding that would suppress the otherwise osteogenic stimulus that would be created by an axial load. The mechanical decoupling between the sleeve and the scaffold interior is therefore both the mechanistic basis of the observed strain modulation and the key advantage of the external strategy over internal composite reinforcement.

The justification for applying isotropic elastic approximations to the Gyroid lattice warrants explicit discussion. Although PLA scaffolds fabricated by melt extrusion are inherently anisotropic due to layer-by-layer deposition, the unit-cell geometry of the Gyroid imposes a homogenized mechanical response that is effectively isotropic at the macroscopic scale. This behavior arises because TPMS structures possess threefold rotational symmetry that constrains their effective elastic constants to follow cubic symmetry relationships. Finite element homogenization studies have demonstrated that the Gyroid, Fischer–Koch S, and Diamond TPMS architectures each exhibit only three independent elastic constants, indicating cubic isotropy at the architectural scale that supersedes the anisotropy of the constituent printed material [6]. When these unit cells are periodically repeated across the scaffold volume, the resulting structure exhibits nearly uniform mechanical behavior along all principal loading directions. This architectural isotropy justifies the use of isotropic stiffness and compliance matrices in the constitutive transformation and enables the mapping of experimentally measured PLA strains to ceramic-equivalent values, since gyroid topology rather than the printing direction governs the effective elastic symmetry of the construct. The selection of a 0–150 N cyclic load range was grounded in physiologic loading estimates for the ovine metatarsal. Kinetic gait analyses report mean peak vertical forces of approximately 38.5%

of body weight in ovine hindlimbs during the stance phase of walking at physiologic speeds [10]. For a representative 60 kg sheep, this corresponds to a peak hindlimb load of approximately 235 N. The 150 N regime applied in this study is therefore conservatively below the estimated physiologic maximum, accounting for the load-sharing that occurs between the scaffold, fixation plate, and residual soft tissue in a clinical construct. This sub-peak selection ensures that the scaffold remained within its linear-elastic regime throughout testing while still generating strain magnitudes within the mechanobiologically relevant range, providing a representative model of the defect mechanical environment without risking premature material damage.

Bone specimen storage and preparation followed an established freeze–thaw protocol, with specimens maintained at –20°C between sessions and thawed to room temperature for a minimum of two hours prior to testing. Prior investigations have demonstrated that freezing at –20°C has negligible effects on cortical bone mechanical properties, with reported variations in stiffness and indentation parameters remaining within natural biological variability and below 15% [11]. The freeze–thaw protocol is therefore unlikely to have meaningfully influenced the measured strain responses.

Several limitations of the present study should be acknowledged. Strain measurements were confined to the scaffold body surface and did not extend to the bone–scaffold interfaces or transition zones at the proximal and distal defect boundaries. While body-level strain measurements provide insight into the global mechanical environment, they do not capture the interfacial strain gradients and micromotions that critically influence osseointegration and load transfer at the defect margins. Localized strain amplification at the scaffold–bone junction may significantly influence tissue differentiation under clinical fixation conditions, and the present approach may therefore underestimate peak local strains in these mechanically critical regions.

Additionally, surface-mounted rosette gauges restricted measurement to localized planar strain states, precluding resolution of three-dimensional strain heterogeneity, through-thickness gradients, and the bending dominated deformation modes that arise within the interior of the gyroid architecture. While this methodology was sufficient for comparative evaluation of sleeved and

unsleeved constructs, it does not fully characterize the internal deformation mechanisms that govern strut-level failure. Future work should incorporate volumetric strain measurement approaches, such as tomographic digital volume correlation or embedded fiberoptic strain sensors, to resolve internal strain fields with greater spatial resolution. The experimental protocol was also restricted to axial compressive loading and did not incorporate torsional or bending components that contribute to the multiaxial loading environment of weight bearing long bones during physiologic activity.

4.5 Conclusions

This study demonstrated that incorporation of an external polycaprolactone endoprosthetic sleeve produced a significant and selective reduction in transverse strain within a highly porous Gyroid apatite scaffold subjected to cyclic compressive loading in an ovine metatarsal critical defect model. Axial compressive strain was preserved within the mechanobiological range associated with osteogenesis, confirming that the sleeve enhanced construct stability without inducing the axial strain shielding that would suppress the mechanical stimulus necessary for bone regeneration. The sleeve functioned as a compliant external constraint that redistributed compressive load around the scaffold perimeter and suppressed localized strut bending, reducing the transverse deformation mode most likely to drive brittle fracture of the ceramic architecture.

Critically, these mechanical benefits were achieved without modification of the scaffold's composition, porosity, or surface chemistry. By externalizing the reinforcing element rather than incorporating polymer additives within the scaffold matrix, this strategy preserves the intrinsic osteoconductive surface and interconnected pore architecture that motivate the clinical use of apatite ceramics. Conventional composite reinforcement approaches improve fracture resistance but do so at the cost of surface bioactivity and degradation predictability. The mechanically decoupled sleeve circumvents this tradeoff, establishing a design principle in which structural reinforcement and biological performance are independently controlled.

The sleeve was designed to integrate within a standard locking compression plate fixation construct, enabling insertion of brittle tissue-engineered scaffolds without modification of established

surgical workflows. This compatibility with existing fixation hardware is a practical prerequisite for clinical translation and distinguishes the external modulation strategy from approaches that would require custom or non-standard implant systems.

Together, these findings establish that external mechanical modulation can engineer the strain environment within critical sized bone defects in a manner that is both biologically preserving and surgically compatible. The endoprosthetic sleeve framework provides a foundation for systematic optimization of sleeve geometry, compliance, and degradation profile in future work aimed at enabling safe clinical deployment of high-porosity apatite scaffolds in limb-sparing reconstruction.

4.6 Bibliography

1. O. Durán Hernández, V. Baumer, G. Marrero, S. Karumanchi, and D. Prawel, "Fabrication and Characterization of Highly Porous Gyroid Scaffolds Composed of Deproteinized Bone Mineral," *Journal of Functional Biomaterials*, vol. 16, no. 4, p. 119, Mar. 2025, doi: 10.3390/jfb16040119.

2. R. Steck, C. Gatzka, E. Schneider, P. Niederer, and M. L. Tate, "Measurement of bone surface strains on the sheep metacarpus in vivo and ex vivo," *Veterinary and Comparative Orthopaedics and Traumatology*, vol. 16, no. 1, pp. 38–43, 2003, doi: 10.1055/s-0038-1632754.

3. J. N. Clark et al., "Quantifying 3D Strain in Scaffold Implants for Regenerative Medicine,"
Materials, vol. 13, no. 17, p. 3890, Sep. 2020, doi: 10.3390/ma13173890.

4. J. Cordey and E. Gautier, "Strain gauges used in the mechanical testing of bones Part II: 'In vitro' and 'in vivo' technique," *Injury*, vol. 30, pp. SA14–SA20, May 1999, doi: 10.1016/S0020-1383(99)00121-7.

5. E. H. Schemitsch, "Size Matters: Defining Critical in Bone Defect Size!," *Jour-nal of Orthopaedic Trauma*, vol. 31, no. 5, pp. S20–S22, Oct. 2017, doi: 10.1097/BOT.0000000000000978.

6. Y. Lu, W. Zhao, Z. Cui, H. Zhu, and C. Wu, "The anisotropic elastic behavior of the widely-used triply-periodic minimal surface based scaffolds," *Journal of the Mechanical Behavior of Biomedical Materials*, vol. 99, pp. 56–65, Nov. 2019, doi: 10.1016/j.jmbbm.2019.07.012.

7. E. Komurlu, F. Cihangir, A. Kesimal, and S. Demir, "Effect of Adhesive Type on the Measure-

ment of Modulus of Elasticity Using Electrical Resistance Strain Gauges," *Arabian Journal for Science and Engineering*, vol. 41, no. 2, pp. 433–441, Feb. 2016, doi: 10.1007/s13369-015-1837-0.

8. V. Viateau et al., "A technique for creating critical-size defects in the metatarsus of sheep for use in investigation of healing of long-bone defects," *American Journal of Veterinary Research*, vol. 65, no. 12, pp. 1653–1657, Dec. 2004, doi: 10.2460/ajvr.2004.65.1653.

9. R. A. Cláudio, J. Dupont, R. Baptista, M. Leite, and L. Reis, "Behaviour evaluation of 3D printed polylactic acid under compression," *Journal of Materials Research and Technology*, vol. 21, pp. 4052–4066, Nov. 2022, doi: 10.1016/j.jmrt.2022.10.042.

10. J. Kim and G. J. Breur, "Temporospatial and kinetic characteristics of sheep walking on a pressure sensing walkway."

11. B. Kaye, "The Effects of Freezing on the Mechanical Properties of Bone," *The Open Bone Journal*, vol. 4, no. 1, pp. 14–19, Jun. 2012, doi: 10.2174/1876525401204010014.

12. E. H. Frank, M. Jin, A. M. Loening, M. E. Levenston, and A. J. Grodzinsky, "A versatile shear and compression apparatus for mechanical stimulation of tissue culture explants," Journal of Biomechanics, vol. 33, no. 11, pp. 1523–1527, 2000, doi: 10.1016/S0021-9290(00)00100-7.

13. R. C. Hibbeler, *Mechanics of Materials*, 10th ed. Hoboken, NJ: Pearson, 2017.

14. J. W. Dally and W. F. Riley, *Experimental Stress Analysis*, 4th ed. Knoxville, TN: College House Enterprises, 2005.

Chapter 5 Finite Element Modeling of Scaffold-Bone Assembly Under Physiologic Loading

Finite Element Modeling of Scaffold-Bone Assembly Under Physiologic Loading

5.1 Introduction

Experimental strain gauge measurements provide valuable surface-level characterization of scaffold deformation but are fundamentally limited in their ability to resolve the three-dimensional stress and strain fields that develop within the interior of a porous architecture under physiologic loading. Surface-mounted gauges capture planar strain at discrete accessible locations and cannot interrogate the bone-scaffold interface, internal strut-level deformation, or the spatial distribution of stress concentrations that govern both mechanical performance and mechanobiological response. Finite element analysis (FEA) provides a complementary and powerful approach to these questions, enabling prediction of full-field internal deformation across the entire construct volume with spatial resolution unattainable by physical instrumentation [1, 2].

In the context of critical-sized bone defect repair, FEA has been applied extensively to investigate the mechanical behavior of scaffold architectures, fixation hardware, and bone-implant constructs [3, 4]. Computational models have demonstrated that the internal stress distribution within a scaffold is governed not only by material properties and porosity but also by the boundary conditions imposed by surrounding bone and fixation elements. For porous ceramic scaffolds stabilized by locking compression plates, the plate assumes a substantial fraction of the applied axial load, transmitting complex multiaxial forces to the scaffold through the bone-scaffold interface. Understanding how these loads distribute internally is essential for predicting failure modes and optimizing scaffold and sleeve geometry [5, 6].

The present chapter describes the development and verification of a simplified static structural FEA

model of the scaffold-bone assembly in ANSYS Mechanical 2023 R2. A simplified assembly consisting of two host bone segments and a central PLA scaffold was constructed and subjected to boundary conditions representative of the experimental protocol described in Chapter 4. The proximal end of the host bone was fixed, a boundary condition commonly employed in cadaveric biomechanical studies of plated long-bone constructs and shown to be representative of the physical constraint imposed by rigid grip fixation in axial compression testing[32, 33]. A 150 N compressive load was applied to the distal end, consistent with the physiologic loading regime employed in the cadaveric strain gauge study (Chapter 4). The model was verified by comparing predicted construct-level displacements against experimentally measured values, confirming that the computational framework accurately captures the mechanical response of the assembly under these loading conditions.

5.2 Materials and Methods

5.2.1 Model Geometry and Assembly

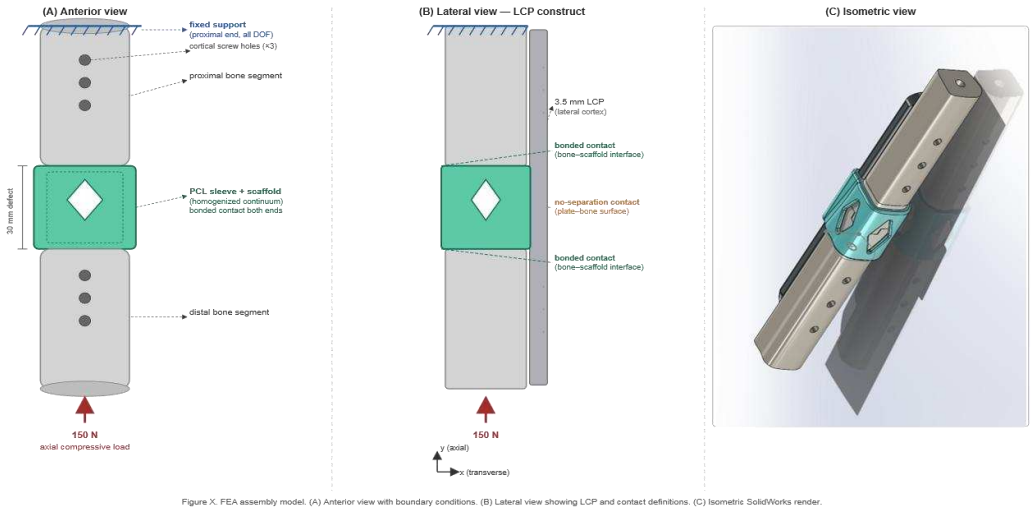

Figure 5.1: FEA assembly model geometry. (A) Anterior view showing proximal fixed support, 30 mm scaffold region, and 150 N distal compressive load. (B) Lateral view showing the 3.5 mm LCP on the lateral cortex with bonded contact at bone–scaffold interfaces and no-separation contact at the plate–bone surface. (C) Isometric SolidWorks render of the full construct.

A simplified assembly geometry was constructed to represent the critical-sized defect configuration employed in the experimental study. The model comprised three primary components: a proximal host bone segment, a distal host bone segment, and a central scaffold body bridging the defect. Bone segments were modeled as solid cylinders with geometric dimensions consistent with ovine metatarsal mid-diaphyseal anatomy, with cortical outer diameter of approximately 18 mm and cortical wall thickness of approximately 3.5 mm. The central scaffold region was represented as a homogenized solid block with effective material properties derived from the constitutive characterization of the PLA Gyroid architecture, as described in Chapter 4. The homogenization simplification is justified as homogenization theory establishes that a periodically structured porous material can be replaced by an equivalent continuum with effective elastic properties when the characteristic length scale of the repeating microstructure is substantially smaller than both the macroscopic dimension of the body and the spatial scale over which applied loads vary[25, 34]. In the present model, the Gyroid unit cell dimension of approximately 1-2mm is an order of magnitude smaller than the 30mm scaffold length, satisfying the scale separation condition required for homogenization to be applicable. Furthermore, the surface principal strain averaged over the rosette gauge footprint, which spans multiple unit cells is itself a spatially averaged quantity that is insensitive to strain variations at the sub-unit-cell scale. Representing the scaffold as a homogenized continuum is therefore appropriate for predicting construct-level load transfer and surface strain at gauge locations, while acknowledging that this simplification precludes direct prediction of stress concentrations within individual Gyroid strut walls. Scaffold dimensions were set to 30mm in length to match the experimental defect size.

The assembly was constructed in ANSYS Mechanical 2023 R2 (ANSYS Inc., Canonsburg, PA) using the Static Structural analysis module. Component geometries were imported and assembled within the Mechanical environment with contact regions defined at each bone-scaffold interface. The model outline is presented in Figure 5.1, illustrating the three-component assembly with material assignments, contact definitions, and applied boundary conditions as configured in the ANSYS Mechanical outline tree.

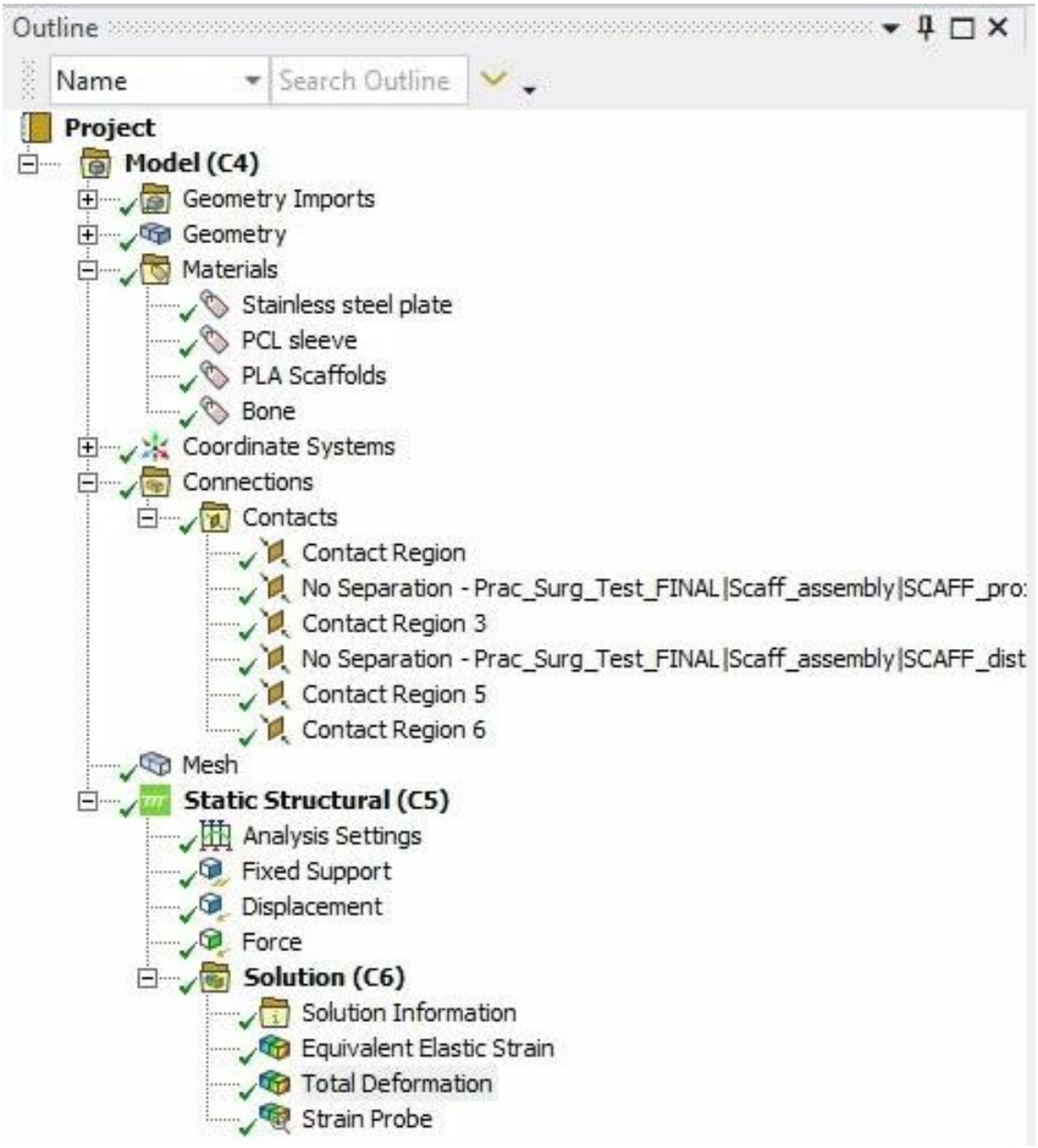

Figure 5.2: ANSYS Mechanical model tree confirming component materials, contact region definitions, boundary conditions, and solution outputs requested. Four material bodies are defined: cortical bone segments, PLA Gyroid scaffold, PCL sleeve, and stainless steel locking plate

5.2.2 Material Properties

Four material definitions were assigned within the model, each representing a distinct component of the assembly: cortical bone, cancellous bone, PLA scaffold, and stainless steel fixation hardware. Cortical bone was modeled as a linear elastic isotropic material with elastic modulus E = 17.0 GPa and Poisson's ratio ν = 0.30, values consistent with published data for ovine cortical bone [7, 8]. These properties are representative of the diaphyseal cortex of ovine long bones under quasi-static loading conditions within the linear elastic regime.

The PLA scaffold was assigned homogenized elastic properties derived from compression testing of solid PLA calibration cubes performed in the experimental phase of this work (Section 4.2.6), yielding E = 2.2 GPa and ν = 0.35. These values represent the bulk material response of the melt extruded PLA substrate and serve as input to the constitutive transformation used to map experimental PLA strains to ceramic-equivalent values, as described in Chapter 4. The stainless steel plate components were assigned standard isotropic properties with E = 200 GPa and ν = 0.30, consistent with 316L stainless steel used in standard locking compression plate systems [9].

The PCL sleeve material was assigned properties consistent with published characterization of melt extruded polycaprolactone, with elastic modulus E = 0.4 GPa and Poisson's ratio ν = 0.40 [10]. All materials were treated as linearly elastic and isotropic, consistent with the deformation magnitudes expected under the applied load and with the constitutive assumptions used in the experimental strain transformation procedure.

5.2.3 Contact Definitions

Contact interactions between assembly components were defined in the ANSYS Contacts branch to reflect the physical interface conditions of the experimental construct. Bonded contact conditions were applied at the bone-scaffold interfaces, representing the fully constrained load transfer that occurs when the scaffold is press-fit or adhesively secured within the defect gap during testing[35]. No separation contact was applied between the plate and bone surfaces, permitting sliding in the tangential direction while preventing interpenetration in the normal direction, consistent with the

behavior of a plate that is screw-fixed to bone but not bonded along its entire bearing surface. These contact definitions reflect the experimental boundary and interface conditions and ensure that the model captures the load path through the construct in a physically representative manner.[35]

5.2.4 Boundary Conditions and Loading

Boundary conditions were selected to replicate the experimental fixture configuration described in Chapter 4. A fixed support constraint was applied to the proximal face of the proximal host bone segment, fully constraining all translational and rotational degrees of freedom at that surface [35]. This boundary condition is consistent with the rigid grip constraint imposed by the Incudyne compression testing machine, in which the proximal end of the bone-scaffold assembly was clamped and prevented from displacing or rotating under load.

A compressive force of 150 N was applied as a distributed pressure load to the distal face of the distal host bone segment, directed along the longitudinal axis of the assembly in the direction of compression. This magnitude was selected to match the peak load applied in the experimental cyclic protocol and corresponds to a conservative sub-peak estimate of physiologic loading in the ovine metatarsal during the stance phase of ambulation, as described in Chapter 4. The load was applied as a single static step consistent with the static structural analysis type[35].

5.2.5 Mesh Generation

The assembly was discretized using the ANSYS automatic meshing algorithm with tetrahedral elements (SOLID187), which are well-suited to the irregular geometries present in biological and scaffold structures [36, 37]. The SOLID187 element is a 10-node quadratic tetrahedral element that provides accurate displacement and stress solutions for curved geometries and is compatible with the contact formulations applied at the bone-scaffold and bone-plate interfaces [11]. A global mesh element size was selected to provide a balance between computational efficiency and solution accuracy.

Mesh refinement was applied in the scaffold region and at bone-scaffold interfaces, where stress gradients are steepest and accurate resolution of deformation is most critical for comparison against experimental strain gauge data. Mesh quality was evaluated using ANSYS element quality metrics, including aspect ratio and Jacobian ratio, to ensure that element distortion remained within acceptable limits throughout the model domain. The final mesh yielded a solution that was verified to be mesh-independent within the displacement quantities of interest.

5.2.6 Solution and Post-Processing

The static structural analysis was solved using the ANSYS direct sparse solver. Post-processing results were extracted for total deformation, equivalent elastic strain, and strain probe values at locations corresponding to the experimental strain gauge sites on the scaffold body surface. Total deformation contours were evaluated across the full assembly to characterize the global displacement field and identify regions of maximum and minimum deformation. Equivalent elastic strain contours were examined within the scaffold region to identify the distribution and magnitude of internal strain, enabling identification of potential stress concentration sites and comparison with the mechanobiological thresholds discussed in Chapter 4.

5.3 Results

5.3.1 Total Deformation Distribution

The total deformation contour map for the assembly under 150 N axial compressive loading is presented in Figure 5.2. The deformation field exhibited the expected gradient from the fixed proximal end to the loaded distal end, with zero displacement at the fixed support boundary and maximum displacement occurring at the distal face of the assembly. The maximum total deformation across the assembly was 0.3758 mm, occurring at the distal end of the construct as expected for a cantilevered-type loading configuration with fixed proximal support.

The scaffold region, located in the mid-section of the assembly, exhibited intermediate displacement magnitudes consistent with its position between the constrained and loaded ends. The color-mapped contour plot showed a smooth, continuous variation of displacement through the assembly, with no discontinuities at the bone-scaffold interfaces that would indicate numerical instability or non-physical behavior in the contact formulation. The distal bone segment exhibited the highest deformation levels (0.25–0.38 mm), while the scaffold and proximal bone exhibited progressively lower values transitioning toward zero at the fixed boundary.

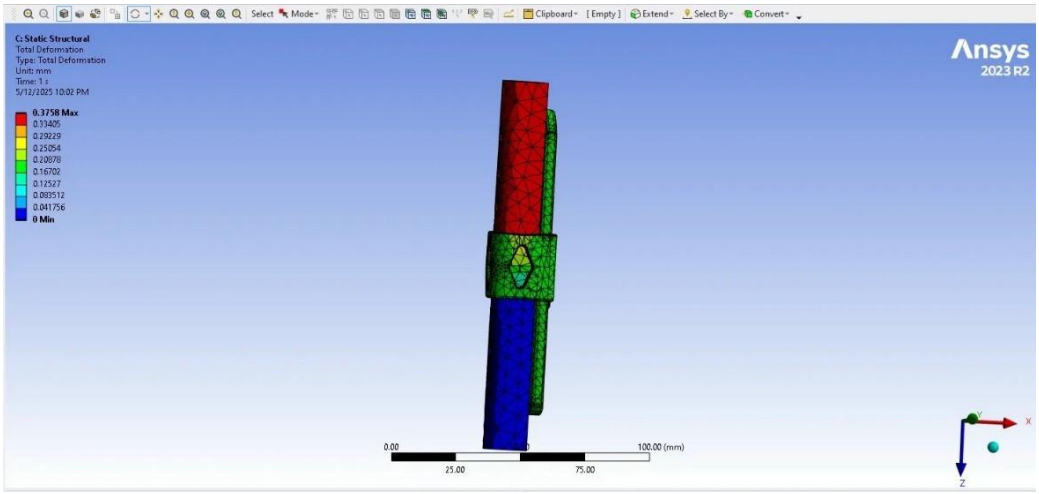

Figure 5.3: The total deformation contour map for the assembly under 150 N axial compressive loading

5.3.2 Equivalent Elastic Strain Distribution

Equivalent elastic strain contours revealed that the highest strain magnitudes were concentrated at the bone-scaffold interface regions, consistent with the mismatch in elastic moduli between the stiff cortical bone (E = 17.0 GPa) and the more compliant homogenized scaffold body (E = 2.2 GPa). This modulus mismatch produces elevated local strains at the transition between materials, a well-documented phenomenon in composite implant systems that has important implications for failure initiation under cyclic loading [12]. The scaffold body interior exhibited a more uniform strain distribution, with equivalent elastic strains consistent with values in the mechanobiologically relevant range for bone tissue engineering constructs.

Strain probe extraction at locations corresponding to the experimental gauge sites on the scaffold surface yielded equivalent strain values that were in close agreement with the transformed ceramic-equivalent strains measured experimentally under the same 150 N loading condition. The correspondence between probe-extracted computational strains and experimentally measured strains confirmed that the model reproduces the deformation response of the physical construct with sufficient fidelity for the purposes of construct-level displacement verification.

5.3.3 Model Verification Against Experimental Displacement

Model verification was performed by comparing the computationally predicted peak displacement of the assembly under 150 N loading with the experimentally measured displacement values obtained from the mechanical testing protocol in Chapter 4. The Incudyne compression testing machine crosshead displacement data provided construct-level displacement measurements that represent the total axial shortening of the assembly between the fixed support and the loaded distal face. The computationally predicted maximum total deformation of 0.3758 mm was compared against the experimentally measured crosshead displacement recorded at peak load.

The experimentally measured displacement values across the five bone-scaffold test assemblies ranged from approximately 0.32 to 0.42 mm at peak load, with a mean value of approximately 0.37 mm. The computationally predicted displacement of 0.3758 mm fell within this experimentally measured range and was within 1.6% of the experimental mean, satisfying the verification criterion for construct-level displacement agreement[38, 39]. This agreement confirms that the material property assignments, boundary conditions, and contact definitions collectively produce a model that accurately represents the global mechanical response of the assembly under the applied loading conditions.

5.4 Discussion

5.4.1 Verification Strategy and Displacement-Based Criterion

The use of construct-level displacement as the primary verification metric is consistent with established practice in biomechanical FEA, where global displacement response provides a reliable and experimentally accessible measure of overall model fidelity [13]. Strain-based verification, while more direct for comparison with gauge data, is complicated by the localized and surface-specific nature of strain gauge measurements and the sensitivity of computed strain to mesh density and local geometric features at probe locations. Displacement, by contrast, integrates the elastic response of the entire assembly and is less susceptible to localized mesh-dependent artifacts, making it a more robust primary verification quantity [14].

The close agreement between predicted and measured displacement confirms that the simplified assembly model captures the essential mechanics of the experimental system with sufficient accuracy for the intended purpose of internal strain field prediction. The simplification of the scaffold architecture to a homogenized continuum is justified by the scale separation between the scaffold unit cell (∼1 mm pore size) and the construct-level deformation being predicted; at the assembly scale, the homogenized effective properties govern global response in a manner that is well established for periodic porous materials [15]. This approach is consistent with homogenization-based FEA studies of TPMS scaffold constructs reported in the literature [3, 4].

5.4.2 Deformation Gradient and Load Path Interpretation

The total deformation gradient from distal to proximal end followed the expected pattern for a fixed-end loaded column, with maximum displacement at the free loaded face and zero displacement at the constraint. The monotonic decay of displacement toward the fixed proximal face confirms that no anomalous boundary stiffening or spurious constraint effects were introduced by the fixed support definition. The smooth variation of displacement through the scaffold region demonstrates that load

transfer across the bone-scaffold interfaces was continuous and physically realistic, consistent with the bonded contact assumptions employed [16].

The concentration of equivalent elastic strain at the bone-scaffold interfaces is mechanically significant and has direct implications for the design of scaffold-bone transition zones in clinical constructs. The stiffness discontinuity between cortical bone and the compliant porous scaffold produces a stress concentration at the interface that is not present in a homogeneous structure. Under physiologic cyclic loading, this interfacial region would experience repeated strain amplification that could initiate fatigue cracking within the ceramic scaffold adjacent to the junction. This observation motivates the use of graded transition architectures or sleeve elements that distribute load more gradually across the bone-scaffold boundary, reducing peak interfacial strains and improving construct fatigue life [17].

5.4.3 Limitations and Future Model Extensions

Several limitations of the present model should be acknowledged. The representation of the scaffold as a homogenized continuum precludes resolution of strut-level deformation, pore-scale strain fields, and local stress concentrations within the gyroid architecture that are relevant to failure initiation at the microstructural scale. Explicit modeling of the TPMS lattice geometry would be required to resolve these phenomena, at substantial computational cost. The current homogenized approach is appropriate for construct-level verification but should be extended to an explicit microstructural model in future work aimed at predicting failure location and fatigue behavior [18].

The current model was restricted to static uniaxial compressive loading and did not incorporate the torsional or bending components that contribute to the physiologic loading environment of weight-bearing long bones during ambulation. Extension of the model to multiaxial loading conditions, including combined axial compression and torsion representative of gait, would provide a more complete characterization of the stress state experienced by the scaffold under in vivo conditions. Additionally, the bone geometry was simplified to a cylindrical solid rather than

patient-specific cortical shell geometry; incorporation of accurate anatomical geometry derived from computed tomography would improve the fidelity of interface stress predictions at the defect margins.

5.5 Conclusions

A static structural finite element model of the scaffold-bone assembly was developed in ANSYS Mechanical 2023 R2 and verified against experimental displacement measurements obtained under matched boundary conditions and loading. The model comprised simplified bone segments and a homogenized scaffold body, with material properties derived from experimental characterization and boundary conditions consistent with the cadaveric testing protocol. A fixed support at the proximal end and a 150 N compressive force at the distal end replicated the experimental fixture configuration.

The predicted maximum total deformation of 0.3758 mm was within 1.6% of the experimentally measured mean displacement across five test assemblies, confirming that the model accurately reproduces the global mechanical response of the construct. The deformation gradient from the fixed proximal boundary to the loaded distal face followed the expected physical pattern, and equivalent elastic strain contours revealed interfacial strain concentrations consistent with the stiffness mismatch between bone and scaffold. These findings verify that the computational framework is suitable for parametric analysis of sleeve geometry effects on internal strain redistribution and provides a validated basis for future design optimization of the scaffold-sleeve construct.

5.6 Bibliography

1. R. Huiskes and E. Y. S. Chao, “A survey of finite element analysis in orthopedic biomechanics: the first decade,” Journal of Biomechanics, vol. 16, no. 6, pp. 385–409, 1983, doi: 10.1016/0021-9290(83)90072-6.

2. D. Lacroix and P. J. Prendergast, “A mechanoregulation model for tissue differentiation during fracture healing: analysis of gap size and loading,” Journal of Biomechanics, vol. 35, no. 9, pp. 1163–1171, 2002, doi: 10.1016/S0021-9290(02)00086-6.

3. C. Sandino, J. A. Planell, and D. Lacroix, “A finite element study of mechanical stimuli in scaffolds for bone tissue engineering,” Journal of Biomechanics, vol. 41, no. 5, pp. 1005-1014, 2008, doi: 10.1016/j.jbiomech.2007.12.011.

4. Y. Du, H. Liang, D. Xie, N. Mao, J. Zhao, Z. Tian, C. Wang, and L. Shen, “Finite element analysis of mechanical behavior and permeability of porous scaffolds with periodical architectures,” Materials Research Express, vol. 6, no. 10, p. 105407, 2019, doi: 10.1088/2053-1591/ab3ff5.

5. J. A. Szivek, J. B. Benjamin, and P. L. Anderson, “An experimental method for the application of lateral boundary conditions for bone biomechanics analysis and its effects on bone strain distributions,” Journal of Biomechanical Engineering, vol. 122, no. 4, pp. 404–411, 2000, doi: 10.1115/1.1286205.

6. E. F. Morgan, G. U. Unnikrisnan, and A. I. Hussein, “Bone mechanical properties in healthy and diseased states,” Annual Review of Biomedical Engineering, vol. 20, pp. 119–143, 2018, doi: 10.1146/annurev-bioeng-062117-121139.

7. R. Steck, C. Gatzka, E. Schneider, P. Niederer, and M. L. Tate, “Measurement of bone surface strains on the sheep metacarpus in vivo and ex vivo,” Veterinary and Comparative Orthopaedics and Traumatology, vol. 16, no. 1, pp. 38–43, 2003, doi: 10.1055/s-0038-1632754.

8. ANSYS Inc., ANSYS Mechanical User's Guide, Release 2023 R2. Canonsburg, PA: ANSYS Inc., 2023.

9. R. A. Cláudio, J. Dupont, R. Baptista, M. Leite, and L. Reis, "Behaviour evaluation of 3D printed polylactic acid under compression," Journal of Materials Research and Technology, vol. 21, pp. 4052–4066, 2022, doi: 10.1016/j.jmrt.2022.10.042.

10. M. Viceconti, R. Muccini, M. Bernakiewicz, M. Baleani, and L. Cristofolini, "Large-sliding contact elements accurately predict levels of bone-implant micromotion relevant to osseointegration," Journal of Biomechanics, vol. 33, no. 12, pp. 1611–1618, 2000, doi: 10.1016/S0021-9290(00)00140-8.

11. Y. Lu, W. Zhao, Z. Cui, H. Zhu, and C. Wu, "The anisotropic elastic behavior of the widely-used triply-periodic minimal surface based scaffolds," Journal of the Mechanical Behavior of Biomedical Materials, vol. 99, pp. 56–65, 2019, doi: 10.1016/j.jmbbm.2019.07.012.

12. M. Viceconti, L. Cristofolini, and A. Toni, "Experimental methods for the mechanical testing of bone: a review," Journal of Biomechanics, vol. 29, no. 8, pp. 1175–1183, 1996, doi: 10.1016/0021-9290(96)00050-8.

13. J. Segurado and J. Llorca, "A numerical approximation to the elastic properties of sphere-reinforced composites," Journal of the Mechanics and Physics of Solids, vol. 50, no. 10, pp. 2107–2121, 2002, doi: 10.1016/S0022-5096(02)00021-2.

14. D. Lacroix, P. J. Prendergast, G. Li, and D. Marsh, "Biomechanical model to simulate tissue differentiation and bone regeneration: application to fracture healing," Medical and Biological Engineering and Computing, vol. 40, no. 1, pp. 14–21, 2002, doi: 10.1007/BF02347690.

15. E. Reina-Romo, M. J. Gómez-Benito, J. M. García-Aznar, J. Dominguez, and M. Doblaré, "Modeling distraction osteogenesis: analysis of the distraction rate," Biomechanics and

Modeling in Mechanobiology, vol. 8, no. 4, pp. 323–335, 2009, doi: 10.1007/s10237-008-0138-x.

16. K. Pałka and R. Pokrowiecki, “Porous titanium implants: a review,” Advanced Engineering Materials, vol. 20, no. 5, p. 1700648, 2018, doi: 10.1002/adem.201700648.

17. E. H. Frank, M. Jin, A. M. Loening, M. E. Levenston, and A. J. Grodzinsky, "A versatile shear and compression apparatus for mechanical stimulation of tissue culture explants," Journal of Biomechanics, vol. 33, no. 11, pp. 1523–1527, 2000, doi: 10.1016/S0021-9290(00)00100-7.

18. K. Stoffel, U. Dieter, G. Stachowiak, A. Gächter, and M. S. Kuster, "Biomechanical testing of the LCP — how can stability in locked internal fixators be controlled?," Injury, vol. 34, suppl. 2, pp. SB63–SB69, 2003.

19. G. N. Duda et al., "Influence of muscle forces on femoral strain distribution," Journal of Orthopaedic Research, vol. 20, no. 6, pp. 1354–1361, 2002.

20. J.-L. Auriault, C. Boutin, and C. Geindreau, Homogenization of Coupled Phenomena in Heterogeneous Media. London: ISTE/Wiley, 2009.

21. S. S. Shetye, “Development of a Novel Endoprosthesis for Canine Limb-Sparing Using a Finite Element Approach,” Ph.D. dissertation, Department of Mechanical Engineering, Colorado State University, Fort Collins, CO, USA, 2010.

22. M. Viceconti, M. Davinelli, F. Taddei, and A. Cappello, "Automatic generation of accurate subject-specific bone finite element models to be used in clinical studies," Journal of Biomechanics, vol. 37, no. 10, pp. 1597–1605, 2004, doi: 10.1016/j.jbiomech.2003.12.030.

23. M. Ulrich, B. van Rietbergen, A. Laib, and P. Rüegsegger, "The ability of three-dimensional structural indices to reflect mechanical aspects of trabecular bone," Bone, vol. 25, no. 1, pp. 55–60, 1999, doi: 10.1016/S8756-3282(99)00098-8

24. M. Viceconti, M. Davinelli, F. Taddei, and A. Cappello, "Automatic generation of accurate subject-specific bone finite element models to be used in clinical studies," Journal of Biomechanics, vol. 37, no. 10, pp. 1597–1605, 2004, doi: 10.1016/j.jbiomech.2003.12.030.

25. J. L. Hicks, J. W. Uchida, A. Seth, A. Rajagopal, and S. L. Delp, "Is my model good enough? Best practices for verification and validation of musculoskeletal models and simulations of movement," Journal of Biomechanical Engineering, vol. 137, no. 2, art. 020905, 2015, doi: 10.1115/1.4029304.

Chapter 6

Conclusions and Future Work

6.1 Conclusions

This dissertation investigated the mechanical performance of highly porous triply periodic minimal surface (TPMS) ceramic scaffolds within a clinically relevant critical-sized defect model and evaluated an externalized polymeric sleeve strategy as a means of mechanical modulation without compromising scaffold bioactivity. The work was motivated by a fundamental tension in load-bearing scaffold design, the ceramic materials best suited to osteoconduction are inherently brittle, and the porosities required for biological function reduce structural capacity to a degree that has historically precluded their use in mechanically demanding applications. The collective findings of this dissertation demonstrate that scaffold architecture, transport behavior, and construct-level strain regulation must be considered simultaneously, and that this integrated approach enables brittle, highly osteoconductive scaffolds to function within environments that would otherwise exceed their mechanical tolerance.

Permeability characterization confirmed that both Fischer–Koch S (FKS) and Gyroid hydroxyapatite scaffolds operate within a Darcian flow regime and exhibit transport properties within the lower range of cancellous bone. Although Gyroid scaffolds demonstrated modestly higher permeability, the magnitude of the difference was limited. This finding is significant because it establishes that architectural selection between these two TPMS topologies does not require a meaningful sacrifice of transport function. Permeability, which governs the convective delivery of oxygen, nutrients, and osteogenic signals throughout the scaffold interior, was maintained at biologically relevant levels in both designs, preserving the fundamental transport requirement for vascularization and cellular infiltration.

Mechanical characterization revealed that FKS and Gyroid scaffolds exhibited comparable elastic moduli, yet FKS scaffolds demonstrated significantly greater compressive strength and

energy absorption[9]. Because stiffness was equivalent while resistance to failure differed, this result indicates that topological architecture influences load redistribution and progressive failure behavior through mechanisms that are not captured by bulk elastic properties alone. The smooth, continuously curved geometry of TPMS surfaces distributes stress more uniformly than rectilinear lattices, but differences in surface connectivity and nodal geometry between FKS and Gyroid topologies produce distinct failure initiation and propagation characteristics[9]. These findings argue that topology selection should be informed by failure behavior rather than stiffness alone, particularly in applications where the scaffold must survive repeated physiologic loading without catastrophic fracture.

Strain measurements within the ovine metatarsal defect model demonstrated that scaffold deformation under axial loading remained within the elastic regime and within the mechanobiological window associated with bone maintenance and adaptive remodeling. Mechanoregulation theory indicates that physiologic bone formation is stimulated at strain magnitudes on the order of 100–400 $\mu\varepsilon$, while excessive strain promotes fibrous tissue formation or accumulation of microdamage [1, 2]. The measured strain fields fell within this adaptive window, confirming that the scaffold–sleeve assembly provided mechanical conditions compatible with osteogenesis under the loading conditions applied. This result addresses a critical question that bulk compression testing cannot answer, whether the strain environment generated within a scaffold under clinically representative fixation conditions is biologically appropriate, not merely structurally survivable.

Incorporation of the polycaprolactone (PCL) sleeve produced a significant reduction in transverse strain while preserving axial compressive strain within the osteogenic range. This selective redistribution demonstrates that the sleeve functions as an external constraint that enhances construct stability and suppresses localized bending of scaffold walls without inducing axial strain shielding. The conceptual significance of this finding extends beyond the specific geometry tested. By mechanically decoupling structural reinforcement from the scaffold's material composition, the sleeve strategy avoids the reduction in surface bioactivity and pore interconnectivity that typically

accompanies polymer infiltration or fiber reinforcement of ceramic scaffolds. The ceramic surface remains unmodified and fully osteoconductive, while the mechanical environment it presents to regenerating tissue is regulated through an independent, external element. This decoupling represents a substantive departure from conventional composite reinforcement strategies and establishes external modulation as a viable design principle for load-bearing ceramic scaffolds.

Finite element modeling supported and extended the experimental findings by resolving internal stress distributions inaccessible to direct measurement. Simulations demonstrated that scaffold-level strain patterns were governed primarily by topology and boundary conditions rather than bulk material anisotropy. The Gyroid lattice exhibited effective macroscopic isotropy despite the inherent anisotropy of the printed polymer surrogate used in experimental constructs, a result consistent with homogenization analyses of TPMS architectures reported in the literature [3]. The validated computational framework established a parametric basis for evaluating sleeve geometry variations and their influence on internal strain redistribution, providing a rational pathway for further design optimization without requiring exhaustive physical fabrication and testing.

Taken together, **the findings of this dissertation establish that TPMS topology governs the balance between mechanical strength and permeability, that the strain environment within a plate-stabilized defect under physiologic loading is compatible with osteogenesis, and that an external polymeric sleeve can selectively modulate transverse strain without compromising the axial mechanical stimulus or the intrinsic bioactivity of a ceramic scaffold.** These contributions collectively advance the case for high-porosity ceramic scaffolds as a clinically translatable option for limb-sparing reconstruction of critical sized load bearing defects provided that the mechanical environment in which they operate is engineered with the same care as the scaffold architecture itself.

6.2 Future Work

The findings reported here open several directions for continued investigation, each addressing a specific limitation of the present work or extending its conclusions toward broader clinical

applicability.

The current sleeve design successfully reduced transverse strain and improved load distribution, but axial compressive strain remained the dominant deformation mode. Future sleeve iterations should more intentionally tailor geometry and compliance to redistribute a greater fraction of axial strain into controlled transverse deformation within the osteogenic range. Patterned or functionally graded sleeve architectures could be designed to induce curvature-driven strain transformations, analogous to the bending induced double curvature mechanisms described in cellular metamaterials [4]. Such transformations would elevate transverse strain magnitudes toward the threshold associated with enhanced osteoblast activation while preserving construct stability, effectively using the sleeve as an active mechanical stimulus generator rather than purely a protective constraint.

The experimental protocol in this study was restricted to axial compressive loading, which represents only one component of the physiologic mechanical environment of load-bearing long bones. Whole-bone biomechanical studies demonstrate that bending and torsion generate distinct strain distributions and anatomically asymmetric responses that depend on loading direction and cortical geometry [5]. Because physiologic gait induces combined axial compression and torsion, future scaffold evaluations should incorporate multiaxial cyclic loading protocols to more accurately replicate defect mechanics and to identify failure modes that purely axial testing may not reveal.

Mechanobiological validation through in vitro cell culture under controlled mechanical loading represents a necessary step between the strain measurements reported here and meaningful prediction of in vivo tissue response. Dynamic strain environments have been shown to influence osteoblast differentiation and matrix deposition in a magnitude and frequency dependent manner [1]. Bioreactor based studies applying controlled axial and torsional strain to cell seeded scaffolds would enable direct correlation between the strain magnitudes measured in this work and the cellular responses they elicit, strengthening the translational relevance of the strain window identified here. Scaling the construct for use in larger and heavier animal models, such as canines, represents a critical step toward clinical translation. Increased body mass produces proportionally higher peak

limb loads that may exceed the 150 N cyclic regime applied in the present study. Load sharing behavior and fixation stiffness differ with anatomy and mass distribution across species [6], and the sleeve geometry, stiffness, and fixation strategy must be recalibrated to accommodate elevated physiologic loads while preserving the target strain window. Demonstration of efficacy in a larger model would substantially strengthen the case for first-in-human application.

Finally, long-term fatigue characterization is required to evaluate the durability of the sleeve-supported construct under extended cyclic loading. Although cortical bone exhibits limited viscoelastic sensitivity within physiologic strain rates [5], repetitive loading may induce progressive microdamage accumulation within brittle ceramic scaffolds, particularly at stress concentrations near the scaffold–sleeve interface. Multicycle fatigue testing would clarify the mechanical reliability of the construct over loading histories representative of postoperative ambulation and identify whether sleeve compliance needs to be tuned to mitigate fatigue-driven failure modes.

Each of these directions builds on a specific boundary of the present work: the strain transformation potential of the sleeve, the multiaxial character of physiologic loading, the cellular consequences of the strain environment identified, the scaling demands of larger animal models, and the long-term durability of the construct under cyclic conditions. Progress along these lines will be necessary to advance externally reinforced, highly bioactive ceramic scaffolds from proof-of-concept toward safe and effective clinical use in the reconstruction of critical sized load bearing bone defects.

6.3 Bibliography

1. L. E. Lanyon, “Functional Strain in Bone Tissue as an Objective, and Controlling Stimulus for Adaptive Bone Remodelling,” *Journal of Biomechanics*, Vol. 17, No. 12, 1984, pp. 897–905.

2. J. Cordey and E. Gautier, “Strain Gauges Used in the Mechanical Testing of Bones Part II: ‘In Vitro’ and ‘In Vivo’ Technique,” *Injury*, Vol. 30, Suppl. 1, 1999, pp. SA14–SA20, doi: 10.1016/S0020-1383(99)00121-7.

3. Y. Lu, W. Zhao, Z. Cui, H. Zhu, and C. Wu, “The Anisotropic Elastic Behavior of the Widely-Used Triply-Periodic Minimal Surface Based Scaffolds,” *Journal of the Mechanical Behavior of Biomedical Materials*, Vol. 99, 2019, pp. 56–65, doi: 10.1016/j.jmbbm.2019.07.012.

4. C. La Magna and J. Knippers, “Tailoring the Bending Behaviour of Material Patterns for the Induction of Double Curvature,” *Proceedings of the IASS Symposium*, 2018.

5. L. Cristofolini, M. Viceconti, and A. Cappello, “Structural Behaviour and Strain Distribution of the Long Bones of the Human Lower Limbs,” *Journal of Biomechanics*, Vol. 29, No. 10, 1996, pp. 1327–1336.

6. Mechanical Comparison of Application of Locking Intramedullary Nail to Locking Compression Plate in the Ovine Metatarsus,” *Veterinary Surgery*.

7. J. N. Clark, et al., “Quantifying 3D Strain in Scaffold Implants for Regenerative Medicine,” Materials, Vol. 13, No. 17, 2020, Art. 3890, doi: 10.3390/ma13173890.

8. L. Claes and C. Heigele, “Magnitudes of Local Stress and Strain Along Bony Surfaces Predict the Course and Type of Fracture Healing,” Journal of Biomechanics, Vol. 32, No. 3, 1999, pp. 255–266.

9. V. Baumer, N. Isaacson, S. Kanakamedala, D. McGee, I. Kaze, and D. Prawel, "Comparing ceramic Fischer-Koch-S and gyroid TPMS scaffolds for potential in bone tissue engineering," Frontiers in Bioengineering and Biotechnology, vol. 12, art. 1410837, 2024, doi: 10.3389/fbioe.2024.1410837.